Chapter 2

Computational Approaches for Plasmonics

M. A. Yurkin[a,b]

[a] *Institute of Chemical Kinetics and Combustion SB RAS, Institutskaya 3 Novosibirsk, 630090, Russia*
[b] *Novosibirsk State University, Pirogova 2 Novosibirsk, 630090, Russia*
yurkin@gmail.com

In this chapter the problem of elastic light scattering, i.e. interaction of electromagnetic waves with finite objects, is discussed. A detailed overview of one of the widely used methods for plasmonics, the *discrete dipole approximation* (DDA), is presented. This includes the theory of the DDA, practical recommendations for using available computer codes, and discussion of the DDA accuracy.

2.1 Introduction

Although the field of plasmonics has experienced a rapid growth in recent decades, it started long before that. In particular, the analytical solution for light scattering by a sphere was developed by Mie [1] to explain the color of colloidal gold. Since then a number of methods to solve Maxwell's equations has been developed [2] mainly motivated by other fields, such as astrophysics

Handbook of Molecular Plasmonics
Edited by F. Della Sala and S. D'Agostino

ISBN 978-981-4303-20-0 (Hardcover), 978-981-4303-21-7 (eBook)
www.panstanford.com

and atmospheric remote sensing [3]. Nowadays, an opposite process is taking place—more and more methods of numerical electromagnetics are applied to nanoparticles.

In this chapter we mainly discuss the problem of *elastic light scattering*, i.e. interaction of electromagnetic waves with finite objects. However, problems involving infinite scatterers, such as surfaces or periodic objects, are also addressed. Other physical processes, such as two-photon or Raman scattering, can be simulated using the near-field distribution obtained during the solution of the light scattering problem. Moreover, this chapter is limited to non-magnetic scatterers.

The first goal of this chapter is to review existing methods to simulate light scattering by plasmonic systems, including the applicability of bulk electric permittivity to nanoparticles. The second goal is to provide a detailed overview of one of the widely used methods, the DDA. This includes the theory of the DDA, practical recommendations for using available computer codes, and discussion of the DDA accuracy.

2.2 Overview of Different Methods

2.2.1 *Finite Scatterers in Homogeneous Medium*

The *Mie theory* [1] and the *T-matrix method* [4] are very efficient for (multilayered) spheres and axisymmetric particles (with moderate aspect ratios), respectively. Several methods, applicable to particles of arbitrary shapes, have been used in plasmonic simulations: the *boundary element method (BEM)* [5, 6], the DDA [7–9], the *finite-difference time-domain method (FDTD)* [10, 11], the *finite element method (FEM)* [12, 13], the *finite integration technique (FIT)* [14] and the *null-field method with discrete sources (NFM-DS)* [15, 16]. There is also quasi-static approximation for spheroids [12], but it is not discussed here.

The BEM, the DDA, the FEM, and the NFM-DS solve the Maxwell's equations in the *frequency domain*. The BEM and the DDA solve by discretization the corresponding surface- and volume-integral equation, respectively. In the FEM the differential form of Maxwell's

equations is solved by volume discretization. The NFM-DS is based on expansion of the electromagnetic field as a combination of spherical wave functions with different centers (so-called, discrete sources), which amplitudes are obtained from boundary conditions at the particle surface.

The FDTD and the FIT solve the *time-domain* Maxwell's equations in the original and modified form, respectively. These two methods, as well as the FEM, need to discretize not only the particle but also some space around it.

There are a few reviews of computational methods in plasmonics [12, 17–19], but none of them aims at full comparison of the methods. General properties of the methods allow one to analyze their scaling properties, e.g. how the simulation time and memory requirements scale with volume of the particle [17]. It does not help, however, in answering the main question: "Given a scattering problem *and required accuracy*, which method is the fastest?" For instance, the variation of refractive index influences computational resources both directly and indirectly through deteriorating accuracy, requiring one to refine discretization.

A systematic comparison of the methods should include the simulation of the several (the more—the better) test problems by these methods running on the same hardware. Such comparisons were performed for dielectric particles, see, e.g. Refs. [20–22], but they are not relevant for the plasmonics. On contrary, in plasmonics such comparisons are very rare. We can cite three examples, which both considered a single specific scattering problem, making it hard to generalize the conclusions. In particular, the FDTD and the FEM were compared for computation of near-field around 50-nm silver cube interacting with 600-nm plane-wave [12]. Accuracy of the FEM was worse than that of the FDTD but still satisfactory. The FEM simulation required 4 hours on a single 3.4 GHz processor, while FDTD—8 hours on 256 double-core 2.6 GHz processors. Another comparison [14] addressed the DDA and the FIT (the latter implemented in the commercial software) for simulation of refractive index sensitivity of rhombic hybrid Au-Ag nanostructure array. Both methods obtained the same value of sensitivity, but the DDA was faster (not specified how much).

The third example [19] is the most systematic one. The DDA, the FEM, and the FDTD were used for the calculation of scattering spectrum of 80-nm gold sphere with several discretizations levels for each method. Unfortunately, the accuracy and simulation times are discussed separately, so it is impossible to say which time corresponds to which accuracy (discretization level). General trend is that DDA is faster but less accurate than the FEM. Simulation time of the FDTD is comparable to that of the FEM, but its accuracy is the worst of three methods. Summarizing all three examples, truly systematic comparisons in these fields will definitely benefit the community.

Finally, the basic configuration for all methods is a finite particle *in vacuum*. However, a scattering problem of a finite particle in homogeneous non-absorbing dielectric medium (with a real refractive index n_0) is equivalent to the basic one after adjusting the wavelength $\lambda \to \lambda/n_0$ and all refractive indices $\tilde{n} \to \tilde{n}/n_0$, due to the corresponding invariance of the frequency-domain Maxwell's equations without sources.

2.2.2 *Periodic Scatterers*

Configurations, obtained by 1D or 2D periodic repetition of a nanoparticle, are common in plasmonics. And most methods can, after some modifications, simulate such configurations, discretizing only one instance of the nanoparticle. Corresponding modifications for the FDTD, the FIT, and the FEM consist in replacing absorbing boundary condition on the outer boundary of the computational domain by a periodic one, see, e.g. Ref. [11].

Modifications required for the BEM and the DDA are more involved. The core entity in these two methods is the Green's tensor, which describes interaction between two discretization elements (e.g. see Eq. (2.6) below for the DDA). To account for particle periodicity, the Green's tensor should be modified to include contributions from all periodic copies of the same discretization element, which involves infinite sums. For the BEM such approach is discussed in Ref. [23], for the DDA in Refs. [24, 25], including implementation in the freely-available computer codes (see Sec. 2.5.4).

2.2.3 *Scatterers Near an Infinite Plane Surface*

Another common configuration in plasmonics is a particle upon or near semi-infinite substrate. This substrate may have no plasmonic properties by itself, e.g. glass, but it still modifies the light scattering properties of the nanoparticle. The FDTD, the FIT, and the FEM can naturally handle such problems, because the effect of the interface is automatically accounted by the part of the substrate falling into the computational domain, when appropriate absorbing boundary conditions are used [11, 13].

The BEM and the DDA can solve this problem discretizing only the particle itself, if the Green's tensor is adjusted to account for the substrate. A resulting Green's tensor is expressed in terms of *Sommerfeld integrals*, accurate evaluation of which is challenging by itself [26]. This has been implemented into the DDA by a number of different researchers [27–30]. Moreover, a simpler way to calculate the Green's tensor in the presence of substrate has been recently proposed by Mackowski [31]. The NFM-DS can also simulate such configurations, taking account of the substrate by additional boundary conditions [16].

Alternative way to approach this scattering problem by the DDA in their standard form is a brute-force discretization of a large block of substrate together with the particle [32, 33]. Finite size of this block does introduce certain artifacts in the computed results. However, they can be diminished by using either the Gaussian beam with size smaller than that of the block [34] or by using empirical compensation formula [32], which also uses result of simulations for truncated substrate without the particle. Similar ideas should, in principle, be also applicable to the BEM.

Finally, periodic scatterers and particles on a substrate, discussed above, are the simplest examples of the scattering problem in a complex background. Real applications may present more elaborate configurations, like multi-layered substrate or periodic array in a film. However, this presents no qualitative difference. In particular, using a proper Green's tensor for the complex background [35], the standard DDA or BEM can be used, discretizing only the scatterer itself.

2.3 Electric Permittivity

There is a consensus that Maxwell's equations work fine for nanoparticles with size down to at least 1 nm. In other words, a good fit of experimental data can be obtained using a rigorous simulation method and proper data for the complex electric permittivity $\tilde{\varepsilon}$ or equivalently the complex refractive index $\tilde{n}$ [36]. This makes choosing a particular value of $\tilde{\varepsilon}$ an important practical question, which can be divided into two parts:

(1) How to choose a correct value of $\tilde{\varepsilon}$ for bulk material?
(2) How the bulk values should be adjusted for small nanoparticles?

First question is a consequence of existence of several sources of data for each material with sometimes significant differences. In particular, for gold there are two widely used sources: by Johnson and Christy [37] and by Palik [38]; however, several other options are also available [7, 36]. Although Khlebtsov [36] provided a prescription based on his experience, choosing the best set of $\tilde{\varepsilon}$ values is still ambiguous. To reliably choose one option over the others one should use a precise experimental data, in which $\tilde{\varepsilon}$ is the most important uncertainty. This strict requirement can, in principle, be complied by single-particle experiments, see, e.g. Ref. [18].

For other plasmonic materials the situation is similar to that of gold. In particular, both sources [37, 38] contain also data for silver and copper. Moreover, handbook by Palik [38] contains data for much more materials with a certain critique justifying the choice of particular values. Some of the known sources for many materials can be found in an online database [39].

Apart from tabulated experimental data, there exist analytical models for the refractive indices. The most widely used is the *Drude free-electron model* [37] (see Sec. 1.2.1):

$$\tilde{\varepsilon}(\omega) = 1 - \frac{\omega_p^2}{\omega\,(\omega + \mathrm{i}/\tau)}\,, \tag{2.1}$$

where ω_p is plasmon frequency and τ is the mean relaxation time. While this model is generally accurate for low frequencies, it is usually not so for $\omega \sim \omega_p$. Therefore, it is not recommended to use

this model in the simulations. The only exception is time-domain methods (e.g. the FDTD), in which only an analytical model for $\tilde{\varepsilon}(\omega)$ can be used, not a set of values. But even then it is recommended to use more elaborate multi-parametric models to better approximate the experimental values of $\tilde{\varepsilon}$ [11].

Second question arises because particles may be comparable or smaller than electron mean free path. Thus, $\tilde{\varepsilon}$, determined mostly by free electrons, is effected by reflections from surface. The common way to include this effect is [36]:

$$\tilde{\varepsilon}(\omega, a) = \tilde{\varepsilon}_b(\omega) + \Delta\tilde{\varepsilon}_{\mathrm{SD}}(\omega, a)\,, \tag{2.2}$$

$$\begin{aligned}\Delta\tilde{\varepsilon}_{\mathrm{SD}}(\omega, a) &= \tilde{\varepsilon}_p^{\mathrm{Dr}}(\omega, a) - \tilde{\varepsilon}_b^{\mathrm{Dr}}(\omega) \\ &= \left[1 - \frac{\omega_p^2}{\omega\left(\omega + \mathrm{i}/\tau_b + \mathrm{i}/\tau_s\right)}\right] - \left[1 - \frac{\omega_p^2}{\omega\left(\omega + \mathrm{i}/\tau_b\right)}\right] \\ &= \frac{\omega_p^2}{\omega\left(\omega + \mathrm{i}/\tau_b\right)} - \frac{\omega_p^2}{\omega\left(\omega + \mathrm{i}/\tau_b + \mathrm{i}/\tau_s\right)},\end{aligned} \tag{2.3}$$

where $\Delta\tilde{\varepsilon}_{\mathrm{SD}}$ is the *surface damping correction*, $\tilde{\varepsilon}_b(\omega)$ is bulk permittivity, a is the size of the nanoparticle, $\tilde{\varepsilon}_b^{\mathrm{Dr}}(\omega)$ and $\tilde{\varepsilon}_p^{\mathrm{Dr}}(\omega, a)$ are bulk and small-particle Drude models respectively, τ_b and τ_s are bulk and *surface-induced damping time* respectively. Surface damping is expressed as [36]:

$$\frac{1}{\tau_s} = \frac{A v_{\mathrm{F}}}{L_{eff}}\,, \tag{2.4}$$

where v_{F} is the Fermi velocity, L_{eff} is the effective electron mean free path, and A is a dimensionless parameter determined by the details of scattering of electrons by the particle surface (which is often simply set equal to 1). Although Eq. (2.4) was originally derived by simple physical, or even geometrical, considerations, later works using ab initio quantum analysis lead to the same result with only difference in value of constant A (reviewed in Ref. [36]).

The only remaining question is dependence of L_{eff} on particle size. For a sphere with radius a, $L_{eff} = a$ and $L_{eff} = 4a/3$ for isotropic and diffuse scattering respectively. For particles of other shapes the following empirical formula can be used $L_{eff} = 4V/S$ [36], where V and S are volume and surface area of the particle, respectively.

Refractive indices of metals, obtained from value of $\tilde{\varepsilon}$ discussed above, vary from moderate values (close to 1 in complex plane) to values with large $\mathrm{Im}[\tilde{n}] = \kappa$ and $|\tilde{n}|$. Although real applications may employ different domains of $\tilde{n}$, in the remainder of this chapter "plasmonic refractive index" denotes the large values of $|\tilde{n}|$. The main motivation for that is that such values of $\tilde{n}$ are the most problematic for the DDA simulation method (see Sec. 2.4.2.1).

2.4 Theory of the DDA

This section is largely based on review [40]. However, it is here restructured and updated with special emphasis given to plasmonic applications.

2.4.1 *General Framework*

We assume $\exp(-\mathrm{i}\omega t)$ time dependence of all fields and that the scatterer is non-magnetic. For simplicity the ω dependence of all quantities is omitted. Quantities indicated with a $\tilde{}$ are complex numbers. Also the electric permittivity $\tilde{\varepsilon}$ is assumed isotropic to simplify the derivations; however, extension to arbitrary dielectric tensors is straightforward. Rigorous derivation of the DDA starts with the *integral equation* governing the electric field inside the finite dielectric scatterer [41, 42]:

$$\begin{aligned}\tilde{\mathbf{E}}(\mathbf{r}) = \tilde{\mathbf{E}}^{inc}(\mathbf{r}) + \int_{V\setminus V_0} \mathrm{d}^3\mathbf{r}'\tilde{\mathbb{G}}^0\left(\mathbf{r},\mathbf{r}'\right)\tilde{\chi}(\mathbf{r}')\tilde{\mathbf{E}}(\mathbf{r}') \\ + \tilde{\mathbf{M}}(V_0,\mathbf{r}) - \mathbb{L}(\partial V_0,\mathbf{r})\tilde{\chi}(\mathbf{r})\tilde{\mathbf{E}}(\mathbf{r})\,, \end{aligned} \tag{2.5}$$

where $\tilde{\mathbf{E}}^{inc}(\mathbf{r})$ and $\tilde{\mathbf{E}}(\mathbf{r})$ are the incident and total electric field at location $\mathbf{r}$, and $\tilde{\chi}(\mathbf{r}) = (\tilde{\varepsilon}(\mathbf{r})-1)/4\pi$ is the susceptibility of the medium at point $\mathbf{r}$. V is the volume of the particle, i.e. the volume that contains all points where the susceptibility is not zero. V_0 is a small volume around $\mathbf{r}$, $\tilde{\mathbb{G}}^0(\mathbf{r},\mathbf{r}')$ is the *free-space Green's tensor*:

$$\tilde{\mathbb{G}}^0\left(\mathbf{r},\mathbf{r}'\right) = \frac{\exp(\mathrm{i}kR)}{R}\left[k^2\left(\mathbb{I}-\frac{\mathbf{RR}}{R^2}\right) - \frac{1-\mathrm{i}kR}{R^2}\left(\mathbb{I}-3\frac{\mathbf{RR}}{R^2}\right)\right], \tag{2.6}$$

where $\mathbb{I}$ is the identity tensor, $k = \omega/c$ is the free-space wave vector, $\mathbf{R} = \mathbf{r} - \mathbf{r}'$, $R = ||\mathbf{R}||$, and $\mathbf{RR}$ is a tensor defined as $(\mathbf{RR})_{\mu\nu} = R_\mu R_\nu$ (μ and ν are Cartesian components). Note that Eq. (2.6) is obtained directly from Eq. (1.213).

$\tilde{\mathbf{M}}$ is the following integral associated with the finiteness of the exclusion volume V_0:

$$\tilde{\mathbf{M}}(V_0, \mathbf{r}) = \int_{V_0} \mathrm{d}^3\mathbf{r}' \left[\tilde{\mathbb{G}}^0(\mathbf{r}, \mathbf{r}')\, \tilde{\chi}(\mathbf{r}')\tilde{\mathbf{E}}(\mathbf{r}') - \mathbb{G}^{st}(\mathbf{r}, \mathbf{r}')\, \tilde{\chi}(\mathbf{r})\tilde{\mathbf{E}}(\mathbf{r}) \right], \tag{2.7}$$

where $\mathbb{G}^{st}(\mathbf{r}, \mathbf{r}')$ is the static limit ($k \to 0$) of $\tilde{\mathbb{G}}^0(\mathbf{r}, \mathbf{r}')$:

$$\mathbb{G}^{st}(\mathbf{r}, \mathbf{r}') = -\frac{1}{R^3}\left(\mathbb{I} - 3\frac{\mathbf{RR}}{R^2} \right). \tag{2.8}$$

$\mathbb{L}$ is the so-called *self-term tensor*:

$$\mathbb{L}(\partial V_0, \mathbf{r}) = -\int_{\partial V_0} \mathrm{d}^2\mathbf{r}' \frac{\widehat{\mathbf{n}}'\mathbf{R}}{R^3}, \tag{2.9}$$

where $\widehat{\mathbf{n}}'$ is an external normal to the surface ∂V_0 at point $\mathbf{r}'$. $\mathbb{L}$ is always a real, symmetric tensor with trace equal to 4π [43], which does not depend on the size of the volume V_0. On the contrary, $\tilde{\mathbf{M}}$ does depend on the size of the volume; moreover it approaches zero when the size of the volume decreases [42] (if both $\tilde{\chi}(\mathbf{r})$ and $\tilde{\mathbf{E}}(\mathbf{r})$ are continuous inside V_0).

A large variety of methods to solve Eq. (2.5) is thoroughly discussed in Ref. [40]. This chapter is devoted to the mainstream DDA, compatible with the fast Fourier transform (FFT) acceleration (Sec. 2.4.2). It is obtained by discretization of Eq. (2.5) on a regular cubical grid [27] by dividing the scatterer into N cubical subvolumes (dipoles) V_i ($i = 1, \ldots, N$). Size of each dipole is d, and its volume $V_d = d^3$. Setting $V_0 = V_i$ and $\mathbf{r} = \mathbf{r}_i$, the center of cube V_i, Eq. (2.5) can be rewritten as:

$$\tilde{\mathbf{E}}_i = \tilde{\mathbf{E}}_i^{inc} + \sum_{j\neq i}^{N} \int_{V_j} \mathrm{d}^3\mathbf{r}' \tilde{\mathbb{G}}^0(\mathbf{r}_i, \mathbf{r}')\tilde{\chi}(\mathbf{r}')\tilde{\mathbf{E}}(\mathbf{r}') + \tilde{\mathbf{M}}(V_i, \mathbf{r}_i) - \mathbb{L}_i\tilde{\chi}_i\tilde{\mathbf{E}}_i, \tag{2.10}$$

where $\tilde{\mathbf{E}}_i = \tilde{\mathbf{E}}(\mathbf{r}_i)$, $\tilde{\mathbf{E}}_i^{inc} = \tilde{\mathbf{E}}^{inc}(\mathbf{r}_i)$, $\tilde{\chi}_i = \tilde{\chi}(\mathbf{r}_i)$, $\mathbb{L}_i = \mathbb{L}(\partial V_i, \mathbf{r}_i)$. Moreover, for this specific (cubic) geometry of V_i and $\mathbf{r}_i$, $\mathbb{L}_i$ is calculated analytically yielding [25]:

$$\mathbb{L}_i = \frac{4\pi}{3}\mathbb{I}. \tag{2.11}$$

The set of Eq. (2.10) (for all i) is exact except for possible errors in replacing V by a set of cubical cells V_i (see Sec. 2.4.3.4). The principal approximating assumptions are:

$$\int_{V_j} \mathrm{d}^3\mathbf{r}'\tilde{\mathbb{G}}^0(\mathbf{r}_i,\mathbf{r}')\tilde{\chi}(\mathbf{r}')\tilde{\mathbf{E}}(\mathbf{r}') = V_d\,\tilde{\mathbb{G}}^0_{ij}\,\tilde{\chi}(\mathbf{r}_j)\,\tilde{\mathbf{E}}(\mathbf{r}_j)\,, \tag{2.12}$$

$$\tilde{\mathbf{M}}(V_i,\mathbf{r}_i) = \tilde{\mathbb{M}}_i\,\tilde{\chi}(\mathbf{r}_i)\,\tilde{\mathbf{E}}(\mathbf{r}_i)\,. \tag{2.13}$$

They state that corresponding integrals linearly depend upon the values of $\tilde{\chi}$ and $\tilde{\mathbf{E}}$ at point $\mathbf{r}_i$ and allow one to rewrite Eq. (2.10) as:

$$\tilde{\mathbf{E}}_i = \mathbf{E}^{inc}_i + \sum_{j\neq i}^{N}\tilde{\mathbb{G}}^0_{ij}V_j\tilde{\chi}_j\tilde{\mathbf{E}}_j + \left(\tilde{\mathbb{M}}_i - \mathbb{L}_i\right)\tilde{\chi}_i\tilde{\mathbf{E}}_i\,. \tag{2.14}$$

The particular expressions for $\tilde{\mathbb{M}}_i$ and $\tilde{\mathbb{G}}^0_{ij}$ determine the quality of the approximation and are discussed in Sec. 2.4.3.2 and Sec. 2.4.3.1. The most widely used method to justify assumptions in Eq. (2.12) and Eq. (2.13) is assuming $\tilde{\mathbf{E}}(\mathbf{r})$ and $\tilde{\chi}(\mathbf{r})$ constant inside each subvolume:

$$\tilde{\mathbf{E}}(\mathbf{r}) = \tilde{\mathbf{E}}_i\ ,\ \tilde{\chi}(\mathbf{r}) = \tilde{\chi}_i\ \ \text{for}\ \ \mathbf{r}\in V_i\ , \tag{2.15}$$

implying:

$$\tilde{\mathbb{M}}_i = \int_{V_i}\mathrm{d}^3\mathbf{r}'\left(\tilde{\mathbb{G}}^0(\mathbf{r}_i,\mathbf{r}') - \mathbb{G}^{st}(\mathbf{r}_i,\mathbf{r}')\right)\,, \tag{2.16}$$

$$\tilde{\mathbb{G}}^0_{ij} = \frac{1}{V_d}\int_{V_j}\mathrm{d}^3\mathbf{r}'\tilde{\mathbb{G}}^0(\mathbf{r}_i,\mathbf{r}')\,. \tag{2.17}$$

Such formulation is equivalent to the method of moments [41] applied to Eq. (2.5), using unit pulse and delta-function (point-matching) as basis and testing functions respectively.

Two equivalent forms of Eq. (2.14) are [41, 44]:

$$\tilde{\mathbf{E}}^{inc}_i = \tilde{\mathbf{E}}^{exc}_i - \sum_{j\neq i}\tilde{\mathbb{G}}^0_{ij}\,\tilde{\alpha}_j\,\tilde{\mathbf{E}}^{exc}_j\,, \tag{2.18}$$

$$\tilde{\mathbf{E}}^{inc}_i = \tilde{\alpha}_i^{-1}\tilde{\mathbf{P}}_i - \sum_{j\neq i}\tilde{\mathbb{G}}^0_{ij}\tilde{\mathbf{P}}_j\,. \tag{2.19}$$

They seek for the *exciting electric fields* (excluding the field by the dipole itself)

$$\tilde{\mathbf{E}}^{exc}_i = \left(\mathbb{I} + \left(\mathbb{L}_i - \tilde{\mathbb{M}}_i\right)\tilde{\chi}_i\right)\tilde{\mathbf{E}}_i\,, \tag{2.20}$$

and the *dipole polarizations*

$$\tilde{\mathbf{P}}_i = \tilde{\mathbb{\alpha}}_i \tilde{\mathbf{E}}_i^{exc} = V_d \tilde{\chi}_i \tilde{\mathbf{E}}_i \,, \tag{2.21}$$

respectively. DDA implementations are mostly related to the dipole polarization of Eq. (2.19) and Eq. (2.21).

The dipole *polarizability tensor* $\tilde{\mathbb{\alpha}}_i$ is defined as:

$$\tilde{\mathbb{\alpha}}_i = V_d \tilde{\chi}_i \left(\mathbb{I} + \left(\mathbb{L}_i - \tilde{\mathbb{M}}_i \right) \tilde{\chi}_i \right)^{-1} = \tilde{\mathbb{\alpha}}_i^{\mathrm{CM}} \left(\mathbb{I} - \tilde{\mathbb{M}}_i \tilde{\mathbb{\alpha}}_i^{\mathrm{CM}} / V_d \right)^{-1} \,, \tag{2.22}$$

where we used Eq. (2.11) and $\tilde{\mathbb{\alpha}}_i^{CM}$ is the *Clausius–Mossotti (CM) polarizability* obtained assuming $\tilde{\mathbb{M}}_i = \mathbb{0}$:

$$\tilde{\mathbb{\alpha}}_i^{\mathrm{CM}} = \mathbb{I} V_d \frac{3}{4\pi} \frac{\tilde{\varepsilon}_i - 1}{\tilde{\varepsilon}_i + 2} \,, \tag{2.23}$$

with $\tilde{\varepsilon}_i = \tilde{\varepsilon}(\mathbf{r}_i)$. Note that Eq. (2.21) follows Eq. (1.270) and, for a sphere, Eq. (2.23) is the effective polarizability of Eq. (1.192).

Solution of system of linear equations in Eq. (2.14), or one of its equivalent forms, constitutes the most challenging computational part of the DDA, discussed in Sec. 2.4.2. All measurable quantities of interest can be computed from the obtained internal (total) fields or dipole polarizations.

Electric fields near or far from scatterers (called *near-fields* and *scattered-fields*, respectively) are obtained directly from Eq. (2.5) for a point $\mathbf{r}$ outside the scatterer, where $\tilde{\chi}(\mathbf{r}) = 0$. After discretization of the scatterer volume it becomes:

$$\tilde{\mathbf{E}}(\mathbf{r}) = \tilde{\mathbf{E}}^{inc}(\mathbf{r}) + \sum_i^N \int_{V_i} \mathrm{d}^3\mathbf{r}' \tilde{\mathbb{G}}^0 \left(\mathbf{r}, \mathbf{r}'\right) \tilde{\chi}(\mathbf{r}') \tilde{\mathbf{E}}(\mathbf{r}') \,, \tag{2.24}$$

similar to Eq. (2.10). To make Eq. (2.24) ready for practical use, approximations similar to Eq. (2.12) should be used

$$\int_{V_i} \mathrm{d}^3\mathbf{r}' \tilde{\mathbb{G}}^0 \left(\mathbf{r}, \mathbf{r}'\right) \tilde{\chi}(\mathbf{r}') \tilde{\mathbf{E}}(\mathbf{r}') = \tilde{\mathbb{G}}_i^0(\mathbf{r}) \tilde{\mathbf{P}}_i \,. \tag{2.25}$$

The simplest possible expression for $\tilde{\mathbb{G}}_i^0(\mathbf{r})$ is:

$$\tilde{\mathbb{G}}_i^0(\mathbf{r}) = \tilde{\mathbb{G}}^0(\mathbf{r}, \mathbf{r}_i) \,. \tag{2.26}$$

For $\mathbf{r} \to \infty$ it is more convenient to use the *scattering amplitude* $\tilde{\mathbf{F}}$ instead of the total electric field $\tilde{\mathbf{E}}$ (see, e.g. Ref. [45]):

$$\tilde{\mathbf{E}}(\mathbf{r}) - \tilde{\mathbf{E}}^{inc}(\mathbf{r}) = \tilde{\mathbf{E}}^{sca}(r\hat{\mathbf{r}}) = \frac{\exp(\mathrm{i}kr)}{-\mathrm{i}kr} \tilde{\mathbf{F}}(\hat{\mathbf{r}}) \,, \tag{2.27}$$

where $\widehat{\mathbf{r}} = \mathbf{r}/r$ is the unit vector in the scattering direction. In particular, Eq. (2.25) and Eq. (1.220) imply:

$$\tilde{\mathbf{F}}(\widehat{\mathbf{r}}) = -\mathrm{i}k^3 \left(\mathbb{I} - \widehat{\mathbf{r}}\widehat{\mathbf{r}}\right) \sum_i^N \tilde{\mathbf{P}}_i \exp\left(-\mathrm{i}k\mathbf{r}_i \cdot \widehat{\mathbf{r}}\right) . \tag{2.28}$$

The DDA is perfectly applicable to any incident field, provided only that its values can be calculated for all $\mathbf{r}_i$. However, for simplicity we further assume a plane incident wave with unit amplitude:

$$\tilde{\mathbf{E}}^{inc}(\mathbf{r}) = \widehat{\mathbf{e}}^{inc} \exp\left(\mathrm{i}k\widehat{\mathbf{k}}^{inc} \cdot \mathbf{r}\right) , \tag{2.29}$$

where $\widehat{\mathbf{k}}^{inc}$ is the incident direction. The amplitude and *Mueller scattering matrices* for direction $\widehat{\mathbf{r}}$ are determined from $\tilde{\mathbf{F}}(\widehat{\mathbf{r}})$ calculated for two orthogonal incident polarizations [46]. Note that $\tilde{\mathbf{F}}(\widehat{\mathbf{r}}) = -\mathrm{i}k\tilde{\mathbb{F}}\left(\widehat{\mathbf{r}}, \widehat{\mathbf{k}}^{inc}\right) \cdot \widehat{\mathbf{e}}^{inc}$, following the definitions of Sec. 1.6.2.

Integral scattering quantities, such as *scattering cross-section* C_{sca} and *extinction cross-section* C_{ext} (see Sec. 1.6.1) can also be obtained from $\tilde{\mathbf{F}}(\widehat{\mathbf{r}})$ [46, 47]:

$$C_{sca} = \frac{1}{k^2} \int_A \mathrm{d}A \left|\left|\mathbf{F}(\widehat{\mathbf{n}})\right|\right|^2 , \tag{2.30}$$

$$\begin{aligned} C_{ext} &= 4\pi k \sum_i^N \int_{V_i} \mathrm{d}^3\mathbf{r}' \mathrm{Im}\left[\tilde{\chi}(\mathbf{r}')\tilde{\mathbf{E}}(\mathbf{r}') \cdot \tilde{\mathbf{E}}^{inc*}(\mathbf{r}')\right] \\ &= \frac{4\pi}{k^2} \mathrm{Re}\left[\left(\widehat{\mathbf{e}}^{inc}\right)^* \cdot \tilde{\mathbf{F}}(\widehat{\mathbf{k}}^{inc})\right] . \end{aligned} \tag{2.31}$$

Absorption cross section C_{abs} is derived directly from the internal (total) fields [47]:

$$C_{abs} = 4\pi k \sum_i^N \int_{V_i} \mathrm{d}^3\mathbf{r}' \mathrm{Im}\left[\tilde{\chi}(\mathbf{r}')\right] \left|\left|\tilde{\mathbf{E}}(\mathbf{r}')\right|\right|^2 , \tag{2.32}$$

which is most commonly approximated using the notion of point dipoles [48],

$$C_{abs} = 4\pi k \sum_i^N \left[\mathrm{Im}\left[\tilde{\mathbf{P}}_i \cdot \tilde{\mathbf{E}}_i^{exc*}\right] - (2/3)\, k^3 \left|\left|\tilde{\mathbf{P}}_i\right|\right|^2\right] , \tag{2.33}$$

to enable practical evaluation. Other alternatives are discussed in Sec. 2.4.3.3. Radiation forces and torques can also be calculated [49–51].

2.4.2 *Numerical Scheme*

2.4.2.1 Iterative methods to solve the linear system

There are two general types of methods to solve linear systems of equations $\tilde{\mathbb{A}}\tilde{\mathbf{x}} = \tilde{\mathbf{y}}$, where $\tilde{\mathbf{x}}$ is an unknown vector and $\tilde{\mathbb{A}}$ and $\tilde{\mathbf{y}}$ are known complex matrix and complex vector, respectively: *direct* and *iterative* [52]. For a general $n \times n$ matrix (in the DDA $n = 3N$) computation time of direct inversion (e.g. LU decomposition) is $O(n^3)$ and storage requirements $O(n^2)$, while computation time for one iteration is $O(n^2)$ [53]. Generally, iterative methods converge in $O(n)$ iterations, and sometimes they do not converge at all. However, in many cases satisfactory accuracy can be obtained after a much smaller number of iterations. In these cases iterative methods can provide significant increases in speed, especially for large n. Moreover, most iterative methods access the matrix $\tilde{\mathbb{A}}$ only through matrix-vector multiplication (sometimes also with the transposed matrix), which allows the construction of special faster routines for calculation of these products (see Sec. 2.4.2.2). Throughout DDA history, mostly iterative methods were employed. At first, they were used to accelerate computations [54], but they also allowed larger numbers of dipoles to be simulated [55], since storage of the entire matrix is prohibitive for direct methods. The most widely used iterative methods in the DDA are *Krylov-space methods*, also known as *conjugate-gradient (CG)* family of methods [53]. A number of studies were devoted to comparison of different iterative methods in DDA simulations [56–60], but it is still hard to identify the most efficient one. In practical applications *bi-CG-stabilized (Bi-CGSTAB)* and *quasi-minimal-residual (QMR)* iterative solvers [53] are most commonly used, as implemented in production codes (see Sec. 2.5.4). However, less tested alternatives of these methods were also proposed [61–63], designed for better convergence in the finite-precision arithmetic. An important advantage of the QMR is that complex-symmetric property of the DDA interaction matrix can be used to halve the number of matrix-vector multiplications [64] (and thus computational time). Assume that the used formulation for $\tilde{\mathbb{G}}^0_{ij}$ retains the symmetry properties of $\tilde{\mathbb{G}}^0(\mathbf{r}_i, \mathbf{r}_j)$, i.e.

$$\tilde{\mathbb{G}}^0_{ij} = \tilde{\mathbb{G}}^0_{ji}\,. \tag{2.34}$$

In particular, this is true for all formulations described in Sec. 2.4.3.1. Then for any of the equivalent systems of DDA equations (Eqs. 2.14, 2.18, 2.19) $\tilde{\mathbb{A}}$ is complex-symmetric if and only if $\tilde{\alpha}_i$ is complex-symmetric for all i. The latter is true for all cases except chiral and non-diagonal anisotropic absorbing materials. Moreover, when $\tilde{\alpha}_i$ is complex-symmetric, it can be decomposed as $\tilde{\alpha}_i = \tilde{\beta}_i^T \tilde{\beta}_i$, leading to the following form of DDA equations [65]:

$$\begin{aligned} &\tilde{\mathbb{A}}\tilde{\mathbf{x}} = \tilde{\mathbf{y}} \quad ; \quad \tilde{\mathbb{A}}_{ij} = \mathbb{I}\delta_{ij} - \tilde{\beta}_i \tilde{\mathbb{G}}_{ij}^0 \tilde{\beta}_j^T \\ &\tilde{\mathbf{x}}_i = \tilde{\beta}_i \tilde{\mathbf{E}}_i^{exc} = \left(\tilde{\beta}_i^T\right)^{-1} \tilde{\mathbf{P}}_i \quad ; \quad \tilde{\mathbf{y}}_i = \tilde{\beta}_i \tilde{\mathbf{E}}_i^{inc}, \end{aligned} \tag{2.35}$$

which is an intermediate one between Eq. (2.18) and Eq. (2.19).

An important part of the iterative solver is preconditioning, which effectively decreases the condition number of the matrix $\tilde{\mathbb{A}}$ and, therefore, speeds up convergence. Although there are a large variety of preconditioners in the literature [53], most of them apply to general dense or sparse matrices. However, any effective preconditioner for the DDA should not significantly modify the block-Toeplitz structure of $\tilde{\mathbb{A}}$ (see Sec. 2.4.2.2). That is why only the simplest Jacobi preconditioner (transforming $\tilde{\mathbb{A}}$ into a matrix with unit diagonal) has been used. For instance, Eq. (2.35) corresponds to Jacobi-preconditioned $\tilde{\mathbb{A}}$ [65]. Number of iterations required for a particular scattering problem is hard to predict a priori; the best estimate is usually provided by empirical data. Still, there are general theoretical results. Rahola [66] showed that the spectrum of the integral scattering operator for any homogeneous scatterer is a line in the complex plane going from 1 to $\dagger\tilde{n}\dagger^2$, except for a small amount of points, corresponding to resonances for the specific size and shape, e.g. so-called Mie resonances for spheres. Based on this he derived an estimate for the optimal (best) reduction factor for any Krylov-space iterative method (norm of the residual is multiplied by this factor every iteration),

$$\gamma = \left| \frac{\tilde{n} - 1}{\tilde{n} + 1} \right|, \tag{2.36}$$

which is especially accurate for particles much smaller than λ, when no above-described resonances are present. Since $\tilde{\mathbb{A}}$ is a discretization of the integral operator, their spectra are similar (see also [56]). Hence, Eq. (2.36) applies to $\tilde{\mathbb{A}}$ as well, although not exactly.

An important consequence of this analysis is that the spectrum of $\tilde{\mathbb{A}}$, and thus convergence should not depend significantly on the discretization. This fact was also confirmed empirically [56, 67, 68]. Budko *et al*. [69] derived optimal value of γ when using the general overrelaxation iterative method. This estimate of γ is similar but always greater than Eq. (2.36), since this stationary iterative method also constructs the solution in the Krylov subspace but not in the most optimal way.

To estimate the required number of iterations N_{iter} one can combine Eq. (2.36) with commonly used value of 10^{-5} for convergence threshold of the iterative solver:

$$N_{iter} \approx \frac{\ln\left(10^{-5}\right)}{\ln\left(\gamma\right)} = \frac{5\ln(10)}{\ln\left|\left(\tilde{n}+1\right)/\left(\tilde{n}-1\right)\right|}. \qquad (2.37)$$

Applicability of Eq. (2.37) is illustrated by comparison with simulation data [67] in Fig. 2.1. Shown data is for nanospheres discretized with 128 dipoles per diameter; however, a particular value of this parameter is not important, as discussed above. More details about these data are given in Sec. 2.6. The estimate describes well the general behavior of N_{iter} versus λ—it is accurate within the factor of two and lies in between the two tested DDA formulations.

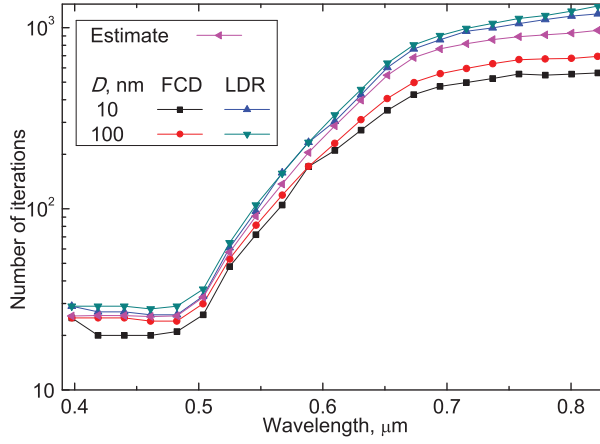

Figure 2.1 Number of iterations for DDA simulations of gold nanospheres (in vacuum) in logarithmic scale. Real data is for two diameters D and two DDA formulations (see Sec. 2.4.3); estimate is based on Eq. (2.37).

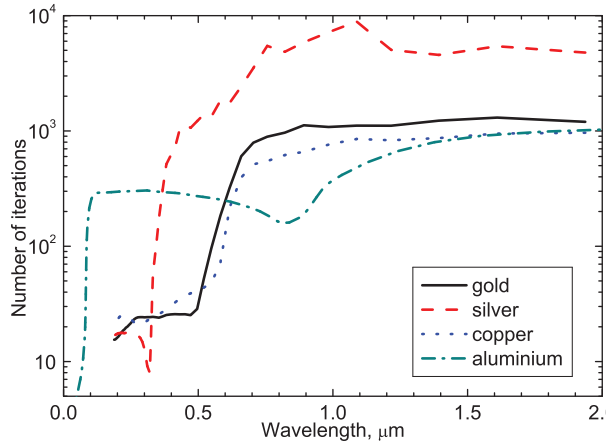

Figure 2.2 Estimated number of iterations, based on Eq. (2.37), for DDA simulations of metallic nanoparticles (in vacuum) in logarithmic scale.

Equation (2.37) is further used to estimate N_{iter} in a wider wavelength range for metals commonly used in plasmonics. The result is shown in Fig. 2.2, using reference refractive index of gold, silver, and copper from [37] and of aluminium from [70]. The general features are small N_{iter} for small λ ($<$ 50–500 nm depending on the metal), much larger and almost constant N_{iter} for large λ ($>$1−1.5 μm), and rapid change somewhere in between. To understand such behavior let us perform an asymptotic expansion of Eq. (2.37) for large $|\tilde{n}|$:

$$N_{iter} \approx \frac{5\ln(10)}{\eta + O(\eta^2)} \approx \frac{5\ln(10)}{2}\frac{1+|\tilde{n}|^2}{\mathrm{Re}[\tilde{n}]}\ ,\ \ \eta = \frac{2\mathrm{Re}[\tilde{n}]}{1+|\tilde{n}|^2}, \qquad (2.38)$$

and apply it to the Drude model (see Eq. (2.1)). In particular, for most metals in the near-infrared the Drude model is accurate and the following limit is satisfied:

$$1/\tau \ll \omega \ll \omega_p \Rightarrow N_{iter}(\omega) \approx 5\omega_p\tau\ln(10)\,. \qquad (2.39)$$

This allows one to quickly estimate N_{iter} for any other metal in the near-infrared using its Drude parameters. Unfortunately, the Drude model is usually inaccurate for $\omega \approx \omega_p$ and, hence, does not provide an accurate estimate of the wavelength position of the transitions in Fig. 2.2. If a nanoparticle is located in dielectric medium

with refractive index $\tilde{n}_0$, the level of the plateau in Fig. 2.2 is $\tilde{n}_0$ times smaller, which follows from Eq. (2.38). Budko and Samokhin [71] generalized Rahola's results to arbitrary inhomogeneous and anisotropic scatterers. Moreover, they described a convex region in the complex plane containing the whole spectrum of the integral scattering operator, including resonances. This region depends only on the values of $\tilde{n}$ inside the scatterer but not on its size and shape. For instance, the size can be comparable or larger than λ. However, size and shape do influence the particular distribution of eigenvalues inside this region; hence, the geometry of the region can be used only to deduce the upper bound of N_{iter}. In particular, for $\tilde{n}$ with zero or small imaginary part this region comes close to the origin, which potentially leads to large N_{iter}. The latter was shown in DDA simulations for real $\tilde{n}$ and large size [59]. Moreover, Ayranci *et al*. [72] observed the decrease of N_{iter} with increasing $\mathrm{Im}[\tilde{n}]$ for sizes comparable with λ. However, for particles much smaller than the wavelength Eq. (2.36) is valid, which has no special behavior for real $\tilde{n}$.

2.4.2.2 Block-Toeplitz structure and FFT acceleration

A square matrix $\mathbb{Q}$ of size $N \times N$ is called *Toeplitz matrix* of order N if $\mathbb{Q}_{ij} = B_{i-j}$, i.e. matrix elements on any line parallel to the main diagonal are the same [52].

In a block-Toeplitz (BT) matrix (of order N_1) elements B_i are not numbers, but square matrices of size $f \times f$ themselves:

$$\mathbb{Q} = \begin{bmatrix} \mathbb{B}_0 & \mathbb{B}_1 & \dots & \mathbb{B}_{N_1-1} \\ \mathbb{B}_{-1} & \mathbb{B}_0 & \ddots & \vdots \\ \vdots & \ddots & \ddots & \mathbb{B}_1 \\ \mathbb{B}_{-N_1+1} & \dots & \mathbb{B}_{-1} & \mathbb{B}_0 \end{bmatrix} \tag{2.40}$$

In a *2-level BT matrix* (of order N_1, N_2) the components $\mathbb{B}_i$ are BT matrices themselves (of order N_2 and size $f \times f$). Proceeding recursively a *M-level BT* (MBT) matrix of order $(N_1, N_2, \dots, N_3)$ and size $f \times f$ for any number of levels can be defined.

Consider a rectangular lattice $n_x \times n_y \times n_z$, numbered in the following way:

$$i = n_y n_z \left(n_x - 1\right) i_x + n_z \left(n_y - 1\right) i_y + n_z i_z, \tag{2.41}$$

where $i_\mu \in \{1, \ldots, n_\mu\}$ indicates the position of the element along the axes. Let us also define the vector index $\mathbf{i} = (i_x, i_y, i_z)$. Then $\tilde{\mathbb{G}}^0_{ij}$, defined by Eq. (2.17), satisfies the following:

$$\tilde{\mathbb{G}}^0_{ij} = \tilde{\mathbb{G}}'_{\mathbf{i}-\mathbf{j}} \tag{2.42}$$

Analogously to Eq. (2.34) it is further assumed that Eq. (2.42) is satisfied for all used formulations for $\tilde{\mathbb{G}}^0_{ij}$. First, Eq. (2.42) can be used to greatly reduce the storage requirements of iterative methods by use of indirect addressing from $O(N^2)$ to $O(N)$. Second, together with Eq. (2.34) it defines a symmetric 3-level BT matrix $\tilde{\mathbb{G}}^0$ (orders of subsequent levels are n_x, n_y, n_z) whose smallest blocks are 3×3 matrices (tensors) $\tilde{\mathbb{G}}^0_{ij}$. The BT-structure can be used for acceleration of direct methods to solve the linear system, which was applied to the DDA by Flatau *et al.* [73, 74]. However, these methods are not discussed here in details due to two major limitations. First, their computational complexity is still larger than that of iterative methods (see below). Second, the whole interaction matrix $\tilde{\mathbb{A}}$ (not only $\tilde{\mathbb{G}}^0$) has to be BT, which is true if and only if polarizabilities of all dipoles in the rectangular grid are the same or, equivalently, the scatterer is homogeneous and rectangular.

The major practical application of the BT-structure is acceleration of matrix-vector product, which is the computational bottleneck of any Krylov-subspace iterative method. Goodman *et al.* [75] showed that multiplication of 3 level BT-matrix $\mathbb{G}$ by a vector can be transformed into a discrete convolution:

$$\tilde{\mathbf{y}}_\mathbf{i} = \sum_{j=1}^{N} \tilde{\mathbb{G}}^0_{ij}\tilde{\mathbf{x}}_j = \sum_{\mathbf{j}=(1,1,1)}^{(n_x,n_y,n_z)} \tilde{\mathbb{G}}'_{\mathbf{i}-\mathbf{j}}\tilde{\mathbf{x}}_\mathbf{j} = \sum_{\mathbf{j}=(1,1,1)}^{(2n_x,2n_y,2n_z)} \tilde{\mathbb{G}}'_{\mathbf{i}-\mathbf{j}}\tilde{\mathbf{x}}'_\mathbf{j}, \tag{2.43}$$

where $\tilde{\mathbb{G}}'_{\mathbf{i}-\mathbf{j}}$ is defined by Eq. (2.42) for $|i_\mu| \leq |n_\mu|$ (and $\mathbb{G}'_\mathbf{0} = \mathbb{0}$) and

$$\tilde{\mathbf{x}}'_\mathbf{j} = \begin{cases} \tilde{\mathbf{x}}_\mathbf{j}\,, & \forall\mu\ 1 \leq j_\mu \leq n_\mu \\ 0\,, & \text{otherwise.} \end{cases} \tag{2.44}$$

Both $\mathbb{G}'$ and $\tilde{\mathbf{x}}'$ are then regarded as periodic in each dimension μ with period $2n_\mu$. A discrete convolution can be transformed by FFT to an element-wise product of two vectors, which is easily computed in $O(N)$ operations. It requires evaluation of a direct and inverse FFT for each matrix-vector product. Each of them is a 3D FFT of

order $2n_x \times 2n_y \times 2n_z$ with $O(N \ln(N))$ complexity. This operation is done for each of the 3 Cartesian components of $\tilde{\mathbf{x}}'$, while FFT of 6 independent tensor components of $\mathbb{G}'$ is done only once during the initialization of the iterative solver.

Alternative methods of FFT acceleration were proposed [73, 76], but the resulting complexity is only slightly different from the one discussed above. It is important to note that for any form of DDA equations [Eqs. 2.14, 2.18, 2.19, 2.35] product of interaction matrix by vector is reduced to product of $\tilde{\mathbb{G}}^0$ by vector through a few $O(N)$ operations, such as element-wise product of two vectors. Therefore, in all these cases the complexity of one iteration of an iterative solver is $O(N \ln(N))$.

As noted above, both the BT-structure and the FFT-acceleration require a cubical lattice of dipoles that completely fills a rectangular box. This has two drawbacks: (1) additional void dipoles should be introduced to build up the grid up to the full box enclosing the particle; (2) position and size of the dipoles cannot be chosen arbitrarily to better describe the shape of the scatterer. These drawbacks are minor for solid and relatively smooth particles, which is usually the case in plasmonics. However, they may become critical for highly porous particles or clusters of particles, where the monomer has a size comparable to a single dipole. Another method to accelerate the DDA computations without the above limitations is the fast multipole method (FMM). It was originally proposed by Greengard and Rokhlin [77] for efficient evaluation of the potential and force fields in N-body simulations. The FMM is based on truncated potential expansions [78] and is principally an approximate method, contrary to FFT-based acceleration. A careful tuning of approximation parameters is important to reach both satisfactory accuracy and low computational complexity. The FMM can be single- or multilevel; the latter is based on hierarchical grouping of particles [79]. The FMM was widely applied in connection with surface-discretization methods [80, 81]. For them the single- and multi-level FMM has complexity of $O(N^{1.5})$ [80] and $O(N \ln^2(N))$ [82], respectively.

The FMM naturally fits the DDA, since the matrix-vector multiplication is actually computing the total field on each single dipole due to all other dipoles [79]. And it was actually implemented

in the framework of the DDA [56, 78, 83]. However, rigorous error analysis (required for the rigorous complexity estimate) is still lacking for the FMM–DDA. Moreover, the multi-level FMM has poor parallel performance, making single-level one more applicable to supercomputers with a large number of cores [80]. Hence, for such hardware performance of the FMM is generally much worse than that of FFT-based methods. Since the FMM is not implemented in any production DDA code, it is not discussed further.

2.4.2.3 Orientation averaging and repeated calculations

In many plasmonic applications one is interested in optical properties of an ensemble of randomly oriented particles. When the concentration of particles is small, multiple scattering is negligible and the optical properties are obtained by averaging single-particle scattering over different particle orientations. Orientation averaging can be described as the integral over the Euler's orientation angles (including a probability distribution function if necessary), which is brought down to a sum by appropriate quadrature. The problem therefore consists in calculation of some scattering property for a set of different orientations of the same particle. The easiest way is to calculate it by solving sequentially and independently each problem from the set. However, the large size of this set calls for some means of reducing the calculations.

Singham *et al.* [84] noted that the set of problems described above is physically equivalent to a fixed orientation of the particle and different incident and scattering directions. Fixed scatterer geometry has two immediate advantages. First, $\tilde{\mathbb{A}}$ is kept constant (although minor variation is possible, see Sec. 2.4.3.2) and need to be computed only once. Second, any scattering quantity (for any angle) is quickly obtained after the linear system is solved for two incident polarizations. Hence, integration over one Euler angle is relatively fast. This finalizes the current state of the art implemented in the production DDA codes. In the following several interesting ideas proposed in the literature are explained, which have not (yet) found a widespread use.

If inverse or *LU* decomposition of $\tilde{\mathbb{A}}$ is available, then scattering problems for each different orientation can be solved in $O(N^2)$

operations [84, 85]. Moreover, analytical averaging over orientations can be performed in $O(N^2)$ operations [84, 86, 87], similarly to the T-matrix method [4]. However, this is still slower than FFT-accelerated iterative methods, when $N_{iter} \ll N$ (which is usually the case).

Another option is to first compute the *T-matrix* of the particle. The T-matrix formalism is based on the multipole expansion truncated at some order n_0, which usually equals to several times size parameter x [88, 89]. The order (number of rows) of the T-matrix equals $2n_0(n_0+2)$. The straightforward way to evaluate the T-matrix based on the DDA is to solve for every incident spherical wave (i.e. for each row of the T-matrix) independently [90] with possible optimization for the repeated calculation discussed above. Using iterative techniques, computation time is $n_0^2 N\left[O(N_{iter}\ln(N)) + O(n_0^2)\right]$, where the first term in the sum is the time for solving the linear system, and the second one is for the computation of the T-matrix components themselves. A new method to obtain the T-matrix from the DDA interaction matrix was proposed by Mackowski [90], requiring two summations with computational time $O(n_0^2 N\ln(N))$ and $O(n_0^4 N)$. For particles larger than λ $O(n_0^4 N)$ usually dominates the computational time of both straightforward and Mackowski's methods, thus decreasing the difference between the two. However, for metallic nanoparticles n_0 can be rather small, while N_{iter} – up to few thousands (see Sec. 2.4.2.1). In this case Mackowski's method to calculate T-matrix will be much faster than the straightforward one, and may prove a faster alternative to calculate orientation-averaged properties. Another class of possible improvements is optimizing multiple runs of iterative solvers with different $\tilde{\mathbf{y}}$. First option is a "heavy" preconditioner, e.g. incomplete factorization preconditioner [53], which has large initialization cost (computed only once) but better convergence rate. Second option is block-iterative methods (see, e.g. [91–93]), which solve the linear system for many $\tilde{\mathbf{y}}$ simultaneously. The main limitation of the latter is significantly larger memory requirements. However, none of these two options have even been tested in the DDA. Okada *et al.* [94] proposed the third option – interpolating the internal field from already simulated orientations to obtain a "good guess" for the initial vector in the simulation

for another orientation. Tests showed that N_{iter} can be decreased several times for a dense grid or orientation angles.

Additionally to performing the DDA simulations for a number of orientations the final accuracy is also affected by the used quadrature (except, when analytical averaging is performed). In the production DDA codes the Simpson rule [95] and the Romberg integration [65] are used, while Okada [96] recently advocated the use of quasi-Monte-Carlo techniques. It is not clear what the best method is, and the answer may depend on a particular problem.

Finally, there are many plasmonic applications requiring DDA simulations for multiple particle sizes (averaging over size distribution) or wavelengths (calculation of a spectrum). Matrix $\tilde{\mathbb{A}}$ depends both on size divided by λ, e.g. x, and $\tilde{n}$. In plasmonics $\tilde{n}$ usually strongly depends on λ. Therefore, simulations for different sizes (or λ) are largely independent. The only known general way to optimize calculations is reusing initial fields from previous simulations to compute a good guess for the iterative solver [97], similarly as was noted above for orientation averaging. However, other improvements are possible in a special case of particles much smaller than the wavelength. Then the interaction matrix for Eq. (2.14) is size-invariant and its part, matrix $\tilde{\mathbb{G}}^0$, is real symmetric. This makes size averaging much easier and simplifies spectrum calculation. First, spectral representation formalism (see [98] for an overview) allows one to reduce the calculation of the whole spectrum to diagonalization of $\tilde{\mathbb{G}}^0$. Second, multiple runs of the iterative solver varying only the refractive index can be significantly optimized using shift-invariance properties of the CG-type iterative methods [99]. Unfortunately, it is hard to specify a size limit for the underlying assumptions to be valid. Usually, size is required to be at least 10 times smaller than all used values [100] of λ. But even stricter requirements may apply for large $|\tilde{n}|$.

2.4.3 *Existing Formulations*

2.4.3.1 Interaction term

Three formulations for the interaction term are known. The simplest is the interaction of point dipoles:

$$\tilde{\mathbb{G}}^0_{ij} = \tilde{\mathbb{G}}^0(\mathbf{r}_i, \mathbf{r}_j)\,. \tag{2.45}$$

The *integrated Green's tensor* (IGT, [101]) is based on a direct numerical integration of Eq. (2.17). This integration takes a lot of time; however, it can be reduced by performing exact calculation only for nearby dipoles, when the difference between Eq. (2.17) and Eq. (2.45) is the largest [65].

The *filtered coupled dipoles* (FCD, [102]) is based on the sampling theory applied to evaluation of the integrals in Eq. (2.5). The electric field and the susceptibility are sampled:

$$\tilde{\chi}(\mathbf{r}')\tilde{\mathbf{E}}(\mathbf{r}') \approx V_d \sum_i h_r(\mathbf{r}' - \mathbf{r}_i)\tilde{\chi}(\mathbf{r}_i)\tilde{\mathbf{E}}(\mathbf{r}_i), \tag{2.46}$$

where h_r is the impulse response function of an *antialiasing filter*:

$$h_r(R) = \frac{\sin(k_F R) - k_F R \cos(k_F R)}{2\pi^2 R^3}\,, \tag{2.47}$$

and $k_F = \pi/d$ is the wavenumber corresponding to the grid. Equation (2.5) is then transformed to Eq. (2.14) with the so-called *filtered free-space Green's tensor*, defined as:

$$\begin{aligned}\mathbb{G}^F_{ij} &= \int_{R^3/V_0} \mathrm{d}^3\mathbf{r}'\tilde{\mathbb{G}}^0(\mathbf{r}_i, \mathbf{r}')h_r(\mathbf{r}' - \mathbf{r}_j) \\ &= \mathbb{I}\left(k^2 g_F(R) + \frac{g_F'(R)}{R} + \frac{4\pi}{3}h_r(R)\right) \\ &\quad + \frac{\mathbf{RR}}{R^2}\left(g_F''(R) - \frac{g_F'(R)}{R}\right)\,,\end{aligned} \tag{2.48}$$

where the symbol $'$ indicates the derivative; the integral is evaluated analytically [102], taking V_0 to be infinitesimally small, and g_F is the *filtered scalar Green's function*:

$$\begin{aligned}g_F(R) = \frac{1}{\pi R}\Big\{ &\sin(kR)\left[\pi\mathrm{i} + \mathrm{Ci}\left((k_F - k)R\right) - \mathrm{Ci}\left((k_F + k)R\right)\right] \\ &+ \cos(kR)\left[\mathrm{Si}\left((k_F + k)R\right) + \mathrm{Si}\left((k_F - k)R\right)\right]\Big\}.\end{aligned} \tag{2.49}$$

To apply this formulation k_F must be larger than k, i.e. $kd < \pi$. But use of the DDA with larger dipoles has little sense anyway. Additional computational time for using the FCD is comparable to a single iteration of the iterative solver, which is negligible in most cases.

The default $\tilde{\mathbb{G}}_{ij}^{0}$, given by Eq. (2.45), is used in almost all applications, while others are considered in only a few papers. However, the effect due to different $\tilde{\mathbb{G}}_{ij}^{0}$ can be much larger than that due to different $\tilde{\alpha}_i$, because the whole matrix $\tilde{\mathbb{A}}$ instead of only its diagonal is affected. For instance, the IGT is known to perform very good for small scatterers with large and almost real refractive indices [101], while the FCD significantly improves the accuracy of the DDA for large $|\tilde{n}|$ [67, 98, 102, 103] (see also Sec. 2.6). Moreover, both the IGT and the FCD may decrease N_{iter} several times in certain cases [98, 101, 103], cutting down the simulation time proportionally. For the FCD this was explained by closer resemblance between spectra of the interaction matrix and the integral scattering operator (see Sec. 2.4.2.1) than that when using CM [98]. It was also proved theoretically that convergence of the IGT with refining discretization for shapes exactly described by a set of cubes is quadratic in kd, contrary to linear convergence of all other DDA formulations except the FCD [104].

Fortunately, all three formulations for the interaction term are implemented in the production codes. So it is recommended to try different options for a particular application, especially when dealing with plasmonic refractive indices.

2.4.3.2 Polarizability prescription

The simplest formula for polarizability (CM) was defined above by Eq. (2.23) and used in the original DDA formulation [54]. All others are equivalent to using non-zero $\tilde{\mathbb{M}}_i$ in Eq. (2.22). The *radiative reaction* correction is based on the radiative damping (see Sec. 1.6.4) of a finite dipole [105]:

$$\tilde{\mathbb{M}}^{\mathrm{RR}} = \frac{2}{3}\mathrm{i}\,(kd)^3\,\mathbb{I}\,. \tag{2.50}$$

It was proposed [48] to satisfy the optical theorem, in particular, to make C_{abs} defined by Eq. (2.33) exactly equal zero for purely real $\tilde{n}$. RR is also included in many other formulae discussed below.

Two other formulations are based on approximate evaluation of Eq. (2.16) replacing the cubical dipole by an equi-volume sphere with radius $a_d = d\,(3/4\pi)^{1/3}$. Obtained result, advocated by

Lakhtakia and others [106, 107], is denoted as LAK,

$$\tilde{\mathbb{M}}^{\mathrm{LAK}} = \frac{8\pi}{3}\mathbb{I}\left[(1 - \mathrm{i}ka_d)\exp(\mathrm{i}ka_d) - 1\right], \tag{2.51}$$

while its series expansion up to the third order of kd was proposed under the name *digitized Green's function* (DGF) [45, 106]:

$$\tilde{\mathbb{M}}^{\mathrm{DGF}} = \mathbb{I}\left(b_1^{\mathrm{DGF}}(kd)^2 + \frac{2}{3}\mathrm{i}(kd)^3\right), \tag{2.52}$$

$$b_1^{\mathrm{DGF}} = (4\pi/3)^{1/3} \approx 1.6111992. \tag{2.53}$$

Peltoniemi [108] improved the LAK formulation by relaxing the assumption in Eq. (2.15). Instead of assuming $\tilde{\mathbf{E}}(\mathbf{r})$ constant inside a dipole it is expanded in Taylor series around the dipole center up to the third order of kr. Then second derivative of $\tilde{\mathbf{E}}(\mathbf{r})$ is expressed in terms of $\tilde{\mathbf{E}}$ itself with help of the Maxwell equations, leading to:

$$\tilde{\mathbb{M}}^{\mathrm{PEL}} = \mathbb{I}\left[b_1^{\mathrm{DGF}}\left(1 + \frac{1}{10}\tilde{n}^2\right)(kd)^2 + \frac{2}{3}\mathrm{i}(kd)^3\right], \tag{2.54}$$

where the assumption of a spherical dipole is also used and $\tilde{n}$ is the refractive index of the point considered.

Another class of polarizability formulations is based not on the integral equation in Eq. (2.5) but on the notion of a set of point dipoles. Draine and Goodman [100] found an optimal $O((kd)^2)$ correction to the CM polarizability in the sense that an infinite lattice of point dipoles with such polarizability would lead to the same propagation of a plane-wave as in a homogeneous medium with a given refractive index. This polarizability was called the *lattice dispersion relation* (LDR):

$$\tilde{\mathbb{M}}^{\mathrm{LDR}} = \mathbb{I}\left[\left(b_1^{\mathrm{LDR}} + b_2^{\mathrm{LDR}}\tilde{n}^2 + b_3^{\mathrm{LDR}}\tilde{n}^2 S\right)(kd)^2 + \frac{2}{3}\mathrm{i}(kd)^3\right], \tag{2.55}$$

$$b_1^{\mathrm{LDR}} \approx 1.8915316,\ b_2^{\mathrm{LDR}} \approx -0.1648469,$$
$$b_3^{\mathrm{LDR}} \approx 1.7700004, \tag{2.56}$$

$$S = \sum_{\mu=x,y,z}\left(\hat{e}_\mu^{inc}\hat{k}_\mu^{inc}\right)^2. \tag{2.57}$$

The LDR prescription can be averaged over all possible incident polarizations [100], resulting in:

$$S = \frac{1}{2}\left(1 - \sum_{\mu=x,y,z}\left(\hat{k}_\mu^{inc}\right)^4\right). \tag{2.58}$$

Later a minor flaw in the LDR derivation was found and corrected [109]. This *corrected LDR* (CLDR) is independent on the incident polarization but leads to a diagonal polarizability tensor instead of scalar:

$$\tilde{\mathbb{M}}^{\mathrm{CLDR}} = \delta_{\mu\nu}\left[\left(b_1^{\mathrm{LDR}} + b_2^{\mathrm{LDR}}\tilde{n}^2 + b_3^{\mathrm{LDR}}\tilde{n}^2\left(\hat{k}_\mu^{inc}\right)^2\right)(kd)^2 + \frac{2}{3}\mathrm{i}\,(kd)^3\right], \tag{2.59}$$

where $\delta_{\mu\nu}$ is the Kronecker symbol.

By construction the LDR is expected to be especially inaccurate near the particle surface. To alleviate this problem Rahmani, Chaumet, and Bryant [110] (RCB) proposed to determine polarizability based on the solution of the electrostatic problem for the same scatterer, described by a tensor $\tilde{\mathbb{D}}(\mathbf{r})$:

$$\tilde{\mathbf{E}}(\mathbf{r}) = \tilde{\mathbb{D}}(\mathbf{r})\tilde{\mathbf{E}}^{inc}. \tag{2.60}$$

Such simple relation is possible only in the static limit, when $\tilde{\mathbf{E}}^{inc}$ does not depend on $\mathbf{r}$. Using Eq. (2.21) and Eq. (2.60) in Eq. (2.19), the latter is exactly satisfied for any $\tilde{\mathbf{E}}^{inc}$ if and only if the following polarizability is used

$$\tilde{\alpha}_i^{\mathrm{RCB}} = V_d\tilde{\chi}_i\tilde{\mathbb{D}}_i\left(\mathbb{I} + V_d\sum_{j\neq i}\mathbb{G}_{ij}^{st}\tilde{\chi}_j\tilde{\mathbb{D}}_j\right)^{-1}, \tag{2.61}$$

where $\tilde{\mathbb{D}}_i = \tilde{\mathbb{D}}(\mathbf{r}_i)$ and $\mathbb{G}_{ij}^{st} = \mathbb{G}_{ij}^{st}(\mathbf{r}_i, \mathbf{r}_j)$. Although the RCB polarizability looks completely different from the CM, they differ significantly only for dipoles closer than $2d$ to the interface [111]. Any $\tilde{\mathbf{M}}$-based polarizability corrections can be further applied to the RCB, replacing $\tilde{\alpha}_i^{\mathrm{CM}}$ by $\tilde{\alpha}_i^{\mathrm{RCB}}$ in Eq. (2.22). For instance, the RR correction was used in the original manuscript [110] and Collinge and Draine [111] applied the CLDR correction leading to the *surface-corrected LDR*.

The RCB has been applied only to simple shapes so far, for which $\tilde{\mathbb{D}}$ is constant (independent of $\mathbf{r}$): spheres, ellipsoids, infinite slabs and cylinders. Application to other shapes is connected with two problems. First, it requires preliminary solution of the electrostatic problem for the same shape, which is not trivial. Second, when $\tilde{\mathbb{D}}$ is not constant the RCB polarizability is generally not symmetric, which is physically impossible in the static case [112]. However, it

is not clear whether this apparent contradiction affects the accuracy of the final results.

Two other polarizability formulations are consequences of formulations for the interaction term (see Sec. 2.4.3.1). In the framework of the FCD [102], the filtered Green's tensor (see Eq. (2.48)) does not have a singularity for zero argument anymore. This can be used for direct evaluation of polarizability [98]:

$$\tilde{\mathbb{M}}^{\mathrm{FCD}} = V_d \lim_{R\to 0} \mathbb{G}^F(\mathbf{R}) = \frac{4}{3}\mathbb{I}\,(kd)^2 + \frac{2}{3}\left(\mathrm{i} + \frac{1}{\pi}\ln\frac{\pi - kd}{\pi + kd}\right)\mathbb{I}\,(kd)^3\,. \tag{2.62}$$

In the framework of the IGT Eq. (2.16) is evaluated numerically to a high accuracy using a *Weyl expansion* of the Green's tensor [101]. However, it is much easier to obtain the series expansion of this result up to the third order of kd. Proceeding similar to the derivation of the DGF but keeping the cubical integration volume one can obtain:

$$\tilde{\mathbb{M}}^{\mathrm{IGT}} = \mathbb{I}\left(b_1^{\mathrm{IGT}}(kd)^2 + \frac{2}{3}\mathrm{i}\,(kd)^3\right), \tag{2.63}$$

$$b_1^{\mathrm{IGT}} = \frac{4}{3}\int_0^1\int_0^1\int_0^1 \frac{\mathrm{d}x\,\mathrm{d}y\,\mathrm{d}z}{\sqrt{x^2+y^2+z^2}}$$

$$= \frac{4}{3}\left[\ln\left(5+3\sqrt{3}\right) - \frac{\ln(2)}{2} - \frac{\pi}{4}\right] \approx 1.586718\,. \tag{2.64}$$

Finally, Dungey and Bohren [113], using results by Doyle [114], proposed to use the electric dipole coefficient $a_1 = -B_1$ (see Sec. 1.6.5) from the Mie theory computed for the inscribed sphere with diameter d and electric permittivity $\tilde{\varepsilon}_s$ determined by the *Maxwell-Garnett effective medium theory* [46]:

$$\frac{\pi}{6}\frac{\tilde{\varepsilon}_s - 1}{\tilde{\varepsilon}_s + 2} = \frac{\tilde{\varepsilon} - 1}{\tilde{\varepsilon} + 2}\,, \tag{2.65}$$

where $\pi/6$ is the volume filling factor. Other effective medium theories may also be used [60]. The dipole polarizability is defined as [114]

$$\tilde{\mathbb{a}}^{Mie} = \mathrm{i}\frac{3}{2k^3}a_1\mathbb{I}\,, \tag{2.66}$$

which recovers the usual polarizability of the sphere (see Sec. 1.6.5). This formulation is denoted as the a_1-term method [115]. It is

expected to be suitable for simulation of clusters of small spheres, where each of them can be modeled by a single dipole.

A large part of the described polarizability prescriptions is implemented in the production codes, namely: CM, RR, LDR, CLDR, DGF, LAK, FCD, IGT. In plasmonic applications dipoles are usually very small, i.e. $kd \ll 1$. This implies that $O((kd)^2)$ differences between the formulations are minor, making the choice of the best prescription not that important. There is, however, an exception. Two prescriptions from the above list, LDR and CLDR, contain terms proportional $(\tilde{n}kd)^2$, which may be significant for not-very-small particles and large $\tilde{n}$ typical in the near-IR. Although LDR is still the most widely used polarizability prescription, its applicability to such $\tilde{n}$ is very debatable, especially for particles larger than λ [98].

2.4.3.3 Calculating measurable quantities

The most widely used way to calculate measurable quantities is using Eqs. 2.26, 2.28, 2.30, 2.31, and 2.33. The major advantage of these equations is that they are exact for the set of point dipoles. Hence, the optical theorem (a consequence of energy conservation), expressed, e.g. as,

$$C_{ext} = C_{abs} + C_{sca}\,, \tag{2.67}$$

is a direct implication of the main DDA equations (e.g. Eq. (2.19)). Therefore, the inaccuracy of Eq. (2.67) is comparable with the final residual of the iterative solver (assuming Eq. (2.30) is evaluated to a high accuracy), which is usually much smaller than the error of the DDA itself (due to other approximations). In particular, Eq. (2.67) can be used for an accurate evaluation of C_{sca} without a laborious integration implied by Eq. (2.30), even when it is up to 100 times smaller than both C_{ext} and C_{abs}.

Other expressions for C_{abs} have also been proposed. Originally, Purcell and Pennypacker [54] used Eq. (2.33) without the second term, but that works satisfactory only in combination with the CM polarizability. Otherwise, physical artifacts occur, such as non-zero C_{abs} for purely real $\tilde{n}$. A more advanced formula was proposed [101] based on radiation correction of a *finite* dipole instead of a *point*

dipole:

$$C_{abs} = 4\pi k \sum_i \mathrm{Im}\left[\tilde{\mathbf{P}}_i \cdot \tilde{\mathbf{E}}_i^*\right], \tag{2.68}$$

which is also a direct approximation to Eq. (2.32). There is no difference between Eq. (2.33) and Eq. (2.68) for the CM, the RR, and the FCD polarizability formulations and also for real refractive indices [40]. Otherwise, the optical theorem is no more exactly satisfied. To alleviate this problem a corresponding correction to C_{ext} was proposed [65]. However, it is not yet clear whether using Eq. (2.68) improves the accuracy of the DDA.

Another possibility is to improve Eq. (2.26) using advanced formulations for the interaction term (Sec. 2.4.3.1). In particular, the following expressions naturally follow from the IGT and the FCD:

$$\tilde{\mathbb{G}}_i^{\mathrm{IGT}}(\mathbf{r}) = \frac{1}{V_d}\int_{V_i} \mathrm{d}^3\mathbf{r}'\tilde{\mathbb{G}}^0(\mathbf{r}_i, \mathbf{r}'), \tag{2.69}$$

$$\tilde{\mathbb{G}}_i^{F}(\mathbf{r}) = \mathbb{G}^F(\mathbf{r}, \mathbf{r}_i). \tag{2.70}$$

These expressions may improve the accuracy of the near-field calculation but, unfortunately, this has never been tested. The production codes allow one to calculate the near-field only using the simplest Eq. (2.26).

The importance of choosing the right expression for $\tilde{\mathbb{G}}_i(\mathbf{r})$ diminishes with increasing r. In particular, it is easy to show that:

$$\tilde{\mathbb{G}}_i^{\mathrm{IGT}}(\mathbf{r}) \overset{r\to\infty}{\longrightarrow} \eta(kd, \widehat{\mathbf{r}})\tilde{\mathbb{G}}^0(\mathbf{r}, \mathbf{r}_i) \tag{2.71}$$

$$\tilde{\mathbb{G}}_i^{F}(\mathbf{r}) \overset{r\to\infty}{\longrightarrow} \tilde{\mathbb{G}}^0(\mathbf{r}, \mathbf{r}_i) \tag{2.72}$$

where

$$\eta\left(x, \widehat{\mathbf{r}}\right) = \prod_{\mu=x,y,z} \frac{\sin\left(\hat{r}_\mu x/2\right)}{\hat{r}_\mu x/2} = 1 - (1/24)\,x^2 + O\left(x^4\right). \tag{2.73}$$

In other words, the FCD does not change the expression for $\tilde{\mathbf{F}}(\widehat{\mathbf{r}})$ given by Eq. (2.28), while the IGT adds the multiplicative factor $\eta\left(kd, \widehat{\mathbf{r}}\right)$, which only slightly differs from unity.

Although all of the described improvements, except those to calculate the near-field, are implemented in the production codes, the default one seems satisfactory. However, further research is required to evaluate possible virtues of the IGT.

2.4.3.4 Decreasing shape errors

The above discussion of different DDA formulations implicitly assumed that particle shape can be exactly described by a set of cubes. Hence, all errors were due to the discretization of the integral equation and related simplifications. In this section so-called shape errors [68] are discussed, which are caused by violation of the above assumption by the real particle shape. First, it is important to note that none of the existing improvements is implemented in the production codes, partly because of the existing internal data structure capable of handling only several different values for polarizabilities of all dipoles [65]. Hence, the main goal of this section is to put forward promising ideas for further development.

A standard way to improve description of the particle shape in numerical solution of integral equations is adaptive discretization, using smaller dipoles near the particle surface. Application of this idea to the DDA is discussed in Ref. [40], but it is incompatible with the FFT acceleration (Sec. 2.4.2.2). Therefore, the only practically viable option is to keep the regular grid of cubical dipoles, but adjust the properties of the boundary dipoles.

Evans and Stephens [50] proposed to modify the susceptibility of the boundary dipole using the Lorentz-Lorenz mixing rule:

$$\frac{\tilde{\chi}_i^e}{4\pi\,\tilde{\chi}_i^e + 3} = f\frac{\tilde{\chi}_i}{4\pi\,\tilde{\chi}_i + 3}, \tag{2.74}$$

where the interface between the particle and vacuum is considered, $\tilde{\chi}_i^e$ is the effective susceptibility, and f is the volume fraction of the subvolume actually occupied by scatterer.

A more advanced averaging, called the *weighted discretization* (WD), was proposed by Piller [116]. It modifies both the susceptibility and the self-term of the boundary dipoles. The particle surface, crossing the subvolume V_i, is assumed linear and divides the subvolume into two parts: the *principal volume* V_i^p that contains the center and a *secondary volume* V_i^s with susceptibilities $\tilde{\chi}_i^p$, $\tilde{\chi}_i^s$ and electric fields $\tilde{\mathbf{E}}_i^p \equiv \tilde{\mathbf{E}}_i$, $\tilde{\mathbf{E}}_i^s$, respectively. Electric fields are considered constant inside each part and related to each other via a boundary condition tensor $\tilde{\mathbb{T}}_i$:

$$\tilde{\mathbf{E}}_i^s = \tilde{\mathbb{T}}_i\tilde{\mathbf{E}}_i. \tag{2.75}$$

Then the total polarization of the subvolume can be evaluated as follows:

$$\tilde{\mathbf{P}}_i = \int_{V_i} \mathrm{d}^3\mathbf{r}'\,\tilde{\chi}(\mathbf{r}')\tilde{\mathbf{E}}(\mathbf{r}') = V_i^{\,p}\tilde{\chi}_i^{\,p}\tilde{\mathbf{E}}_i^{\,p} + V_i^{\,s}\tilde{\chi}_i^{\,s}\tilde{\mathbf{E}}_i^{\,s} = V_d\tilde{\chi}_i^{\,e}\tilde{\mathbf{E}}_i\,, \qquad (2.76)$$

with an effective (averaged) susceptibility:

$$\tilde{\chi}_i^{\,e} = \left(V_i^{\,p}\tilde{\chi}_i^{\,p}\mathbb{I} + V_i^{\,s}\tilde{\chi}_i^{\,s}\tilde{\mathbb{T}}_i\right)/V_d\,. \qquad (2.77)$$

The susceptibility of the boundary subvolume is replaced by an effective one. The effective self-term is evaluated directly starting from Eq. (2.7), considering $\tilde{\chi}$ and $\tilde{\mathbf{E}}$ constant inside each part:

$$\tilde{\mathbb{M}}_i^{\,e}\,\tilde{\chi}_i^{\,e} = \int_{V_i^{\,p}} \mathrm{d}^3\mathbf{r}'\left(\tilde{\mathbb{G}}^0(\mathbf{r}_i,\mathbf{r}') - \mathbb{G}^{st}(\mathbf{r}_i,\mathbf{r}')\right)\tilde{\chi}_i^{\,p} + \int_{V_i^{\,s}} \mathrm{d}^3\mathbf{r}'\left(\tilde{\mathbb{G}}^0(\mathbf{r}_i,\mathbf{r}') - \mathbb{G}^{st}(\mathbf{r}_i,\mathbf{r}')\right)\tilde{\chi}_i^{\,s}\tilde{\mathbb{T}}_i\,. \qquad (2.78)$$

Piller [116] evaluated the integrals in Eq. (2.78) numerically. The polarizability is obtained from Eq. (2.22) using $\tilde{\chi}_i^{\,e}$ and $\tilde{\mathbb{M}}_i^{\,e}\,\tilde{\chi}_i^{\,e}$, while Eq. (2.19) remains unchanged. Hence, the WD does not modify the general numerical scheme. A significant improvement of DDA accuracy due to the WD was shown both by theoretical analysis [104] and in sample simulations [103, 116].

Two other improvements are not aimed exclusively at shape errors, but they affect only dipoles close to the boundary. The first one is the RCB formulation discussed in Sec. 2.4.3.2. Second one is the spectral filtering of $\tilde{\chi}$ that was proposed in combination with the FCD [102] to smooth the change of $\tilde{\chi}$ at the particle boundary by removing high-frequency components.

2.5 Practical Aspects of DDA Simulations

2.5.1 *General Applicability*

The principal advantage of the DDA is that it is completely flexible regarding the geometry of the scatterer, being limited only by the need to use the dipole size d small compared to both any structural

length in the scatterer and λ. For particles with size comparable to or larger than λ the following rule of thumb is commonly used [40]:

$$d = \lambda/10\,|\tilde{n}|\,. \tag{2.79}$$

It implies that the number of dipoles N increase with both size and $\tilde{n}$. The expected accuracy of cross sections is then several percents, if $\tilde{n}$ belongs to the well-tested range, approximately described as

$$|\tilde{n} - 1| < 2. \tag{2.80}$$

For larger $\tilde{n}$ the accuracy of the simulation with default dipole size deteriorates, and smaller, hence more dipoles must be used to improve it. However, there is no strict limitation on $\tilde{n}$ – accurate results can be obtained for a wide range of $\tilde{n}$, given enough computational resources. In this respect state-of-the-art DDA formulations (Sec. 2.4.3) can be of great help.

For particles smaller than λ, e.g. nanoparticles, Eq. (2.79) is definitely not relevant. In this case the main requirement for d is that it should be small enough to resolve fine details of particle shape. For instance, for a compact shape (like sphere or cube) it is recommended to use at least 10 dipoles along the smallest dimension, no matter how small the particle is. Therefore, for nanoparticles N is almost independent of size. However, N does depend on $\tilde{n}$, which is critical due to the wide range of $\tilde{n}$ used in plasmonic applications. In more details these issues are discussed in Sec. 2.6.

2.5.2 *System Requirements*

The major price paid for versatility of the DDA is its large computational costs, even for simple scatterers. The most important factor is the number of dipoles N, which determines both memory requirements M and computational time of one iteration t_{iter}. More precisely, the relevant quantity is the number of dipoles composing the enclosing rectangular box (see Sec. 2.4.2.2), which is typically one-two times larger than N (for compact particles). System requirements largely vary depending on the particular DDA code, arithmetic precision, and iterative solver. The following are the

guiding values:

$$M \approx 1000N \text{ bytes}, \tag{2.81}$$

$$t_{iter} \approx 3 \times 10^{-7} N \ln(N)\, s. \tag{2.82}$$

The latter is an estimate when using a single core of a modern processor. More accurate estimates can be found in the manuals of particular codes (see Sec. 2.5.4).

Required memory is the major factor limiting N when a DDA simulation is run on a single PC. This limitation can be alleviated by parallelization of a single simulation among a cluster of computers, which is implemented in some of the DDA codes. Corresponding parallel efficiency is generally close to unity [65, 117], which means that M is effectively distributed among several computers and t_{iter} is decreased proportionally to the total number of processor cores. However, for efficient parallelization the number of cores must not be greater than the maximum number of dipoles along a coordinate axis.

Total time t of DDA simulation can be decomposed into the following parts:

$$t \approx t_{init} + N_{or} \left(N_{iter} t_{iter} + t_{quan} \right) , \tag{2.83}$$

where t_{init} and t_{quan} are time of initialization and calculation of measurable quantities, respectively, and N_{or} is the number of distinct particle orientations (see Sec. 2.4.2.3). Generally, t_{init} is comparable to t_{iter} and t_{quan} is even smaller. However, the latter is proportional to the number of considered scattering angles or near-field probe points and, thus, may become large in certain conditions. Existing theory concerning N_{iter} is discussed in Sec. 2.4.2.1, here we only note that it is also sensitive to the used arithmetic precision. Using single instead of double precision halves M, but increases round-off errors, which in turn accumulate and increase N_{iter}, especially when the latter is already large.

2.5.3 *Free Parameters*

Many parameters of the DDA codes are directly determined by a scattering problem to be simulated. However, there are also some free parameters that can be tuned. In the following they are listed in the order of decreasing importance:

- the level of discretization (i.e. size or number of dipoles),
- DDA formulation,
- the number of orientations for orientation averaging,
- iterative solver and convergence threshold,
- the volume correction.

The level of discretization is a result of compromise between accuracy and required computational resources. In many cases the required accuracy is specified *a priori*, but finding an appropriate d (or N) is not an easy task. Existing benchmark studies are discussed in Sec. 2.6, but their coverage of the field of plasmonics is relatively poor. Therefore, whenever one plans to run more that a single DDA simulation for a class of similar particles, it is recommended first to perform an accuracy study. For that one should choose a single test particle and perform DDA simulations with different d around the values typically used for similar simulations in the literature. The estimate of d required for a particular accuracy can be obtained from a variation of results with decreasing d. Moreover, the estimation can be made much more rigorous by using an extrapolation technique, as proposed by Yurkin *et al.* [68] and applied in Ref. [67, 98, 118] (see also Sec. 2.6). Seeking a careful compromise is important due to a steep dependence of N (and t) on required accuracy. In particular, two-fold decrease of simulation error usually requires eight-fold increase of N [68, 104].

Different DDA formulations are discussed in Sec. 2.4.3 together with some practical recommendations. The number of orientations required for accurate orientation-averaged results is also hard to estimate *a priori*, since this issue is rarely discussed in details [96, 119]. However, contrary to the DDA simulation itself, it is relatively easy to estimate the accuracy of the orientation averaging during the process and increase the number of orientations, if needed. In other words, orientation averaging can be performed in semi-automatic adaptive regime [65, 96]. Moreover, the dependence of t on accuracy of orientation averaging is not that steep as discussed above for DDA simulation for fixed orientation. Therefore, it may be acceptable to use "large enough" number of orientations.

Different iterative solvers are discussed in Sec. 2.4.2.1 and there are several of them, which work fine in most cases. The convergence

threshold is usually chosen small enough to introduce negligible errors, because in this case the extra accuracy is especially cheap. Convergence of the iterative solver is usually linear in logarithmic scale, so, e.g. ten-fold increase of the typical threshold value of 10^{-5} decreases t by only about 20%. Nevertheless, such acceleration can be useful for very long simulations.

Discretization of a particle in the framework of the DDA is usually performed by testing the dipole centers for belonging to the particle volume. Then the total volume of the set of dipoles differs from volume of the particle. The *volume correction*, implemented and used by default in some DDA codes, changes the size of each dipole (scales the whole set of dipoles) to remove this difference. This is believed to increase the accuracy of DDA, especially for small scatterers, although the effect is not always beneficial [44]. However, in plasmonic applications N is usually large (to get satisfactory accuracy), which decrease the effect of volume correction.

To conclude, although DDA is one of the most conceptually simple and easy-to-use methods to simulate light scattering, performing accurate and fast DDA simulations is still, to some extent, an art. It requires one to consider open questions that still remain, because the plasmonics is a relatively new application domain of the DDA. Hence, to perform reliable and efficient DDA simulations one should take a critical attitude towards results and be ready to experiment with free parameters, instead of hoping for "black box" to produce correct results by itself. Although the DDA codes usually have some built-in empirics to set up the free parameters without any input from user, these empirics may be completely inappropriate in some cases. Finally, in the art of DDA simulations an advice from more experienced users can be invaluable. Apart from traditional means, such advice can also be obtained through an internet discussion group [120].

2.5.4 *Available Codes*

To our knowledge, there exist four freely-available DDA codes: DDSCAT [44], ADDA [65], OpenDDA [117], and DDA-SI toolbox [27]. More DDA codes exist, and some of them are discussed in Ref. [119], but these are not freely available to the community. OpenDDA

and DDA-SI toolbox have been released only recently and not yet well-tested by the community, but they do have attractive features. OpenDDA contains highly-optimized computational kernel which can run efficiently both on multicore processors using OpenMP [121] and on computer clusters using MPI (message passing interface [122]). This is probably the fastest DDA code when using the standard formulation of the DDA. DDA-SI toolbox can rigorously handle particles near the surface (see Sec. 2.2.3) but, unfortunately, do not employ FFT acceleration.

In the following two mature codes are compared, based on their current versions: DDSCAT 7.2 [123] and ADDA 1.1 [124]. However, one should refer to the corresponding manuals [95, 125] for more details. Both codes are fast, accurate and feature-rich, so only the differences are pointed out.

- **DDA formulations.** DDSCAT can rigorously handle 1D and 2D periodic scatterers (see Sec. 2.2.2). ADDA implements state-of-the-art DDA formulations, in particular, the IGT and the FCD (see Sec. 2.4.3.1).
- **Portability.** DDSCAT is written in Fortran 90, while ADDA is written in C99. Both are highly portable and can be compiled on a wide variety of platforms. Additionally DDSCAT developers provide compiled binaries for 32-bit Windows, while ADDA – both for 32-bit and 64-bit Windows.
- **Use of modern hardware.** DDSCAT uses OpenMP to effectively run on multi-core processors and can use MPI to parallelize orientation averaging. ADDA parallelizes a *single* DDA simulation using MPI. Hence, huge N (very large particles or very fine discretization) can be used when running on a large computer cluster. However, for a single multi-core processor the performance of MPI is generally worse than that of OpenMP. Also ADDA features GPU-acceleration, which potentially allows about 10 times acceleration using modern graphics cards.
- **Speed.** The speed of the codes on the same basic hardware can also differ due to differences in algorithms and optimizations. In 2007 Penttila *et al.* [119] compared, among other codes, DDSCAT 6.1 and ADDA 0.7a. ADDA was from

1.2 to 4 times faster than DDSCAT for simulation of light scattering by cubes and spheroids in fixed orientation. However, performance of both codes has been significantly improved since that comparison In particular, DDSCAT currently includes a fast FFT-based routine to calculate near-field [126].

- **Orientation averaging.** DDSCAT employs the Simpson rule as a quadrature for orientation averaging, while ADDA – the Romberg integration. The latter is potentially more accurate and can be used in adaptive regime. However it requires more careful consideration to be used efficiently, and is less flexible in the choice of number of orientations [119].
- **Spectrum calculation.** DDSCAT completely automates calculations for a spectrum of wavelengths in a convenient manner. ADDA can perform such automatic calculations only with the help of additional scripts.
- **User interface.** DDSCAT accepts most of the simulation parameters through a special file. ADDA accepts such parameters through a command line, which is more convenient for scripted parallel runs [119]. However, both codes also use large input files, e.g. to describe an arbitrary particle. Also ADDA features a built-in help system, which should be especially useful for new users.
- **History and development process.** First version of DDSCAT was publicly released in 1993; hence, it is an extremely well-tested and reliable code. In particular, it was used in several hundreds of journal papers. Development of ADDA started in 1990, but the first public release was in 2006. It is also well-tested, exemplified by its use in more than 80 journal papers. Currently ADDA features an open development process with several developers from different countries.

2.6 Accuracy of the DDA

First, it should be stressed that although the name of DDA contains "approximation" due to historical reasons, it is a numerically exact

method in the sense that accuracy can be made however good given enough computational resources. The only limitation on the achievable accuracy is enforced by the machine precision. The proof of DDA numerical exactness was provided by the rigorous convergence analysis [104] based on the derivation of the DDA from the Maxwell's equations using no physical approximations (see Sec. 2.4.1). It was also confirmed by many numerical convergence studies, see, e.g. Refs. [72, 104], also for very large $|\tilde{n}|$ [67, 98, 127].

Accuracy of the DDA in general is discussed in review [40] as well as in more recent benchmark study [72]. However, they are mostly limited to the moderate range of $\tilde{n}$ (see Eq. (2.80)), for which the rule-of-thumb is commonly used (see Sec. 2.5.1). Use of the DDA in plasmonics is mainly application-driven with, unfortunately, little attention paid to error analysis of the DDA itself. Moreover, even in the recent plasmonic papers the DDA is sometimes (e.g. Ref. [12]) wrongly regarded as an approximate method (see the discussion above). This misconception may be caused by two reasons. First, the DDA accuracy for plasmonic $\tilde{n}$ is indeed much worse than for moderate $\tilde{n}$ in the sense that corresponding computational resources needed to achieve the same accuracy are larger. Hence, for some plasmonic applications good DDA accuracy cannot be achieved on, e.g. standard desktop PC. Second, the DDA accuracy is often judged by comparison with experiment, which is also largely affected by uncertainties in the proper values of $\tilde{n}$ (see Sec. 2.3) and in experimental conditions, e.g. in particle shape [128, 129]. So in the following existing literature data on DDA accuracy for metallic nanoparticles is reviewed with particular emphasis on gold. However, the results for other metals are expected to be similar with corresponding changes in λ, because of similar variation ranges of $\tilde{n}$ (see Section 2.4.2.1).

The accuracy of the DDA for gold nanoparticles is usually quoted as "good enough if a large enough number of dipoles is used", i.e. the discussion is qualitative with no error measurements available [130–133]. In a couple of papers DDA results are plotted together with exact reference results in the same graph for spheres [131] and spheroids [132]. These graphs show that errors of extinction efficiency at particular wavelengths can be as large as 50%. Moreover, a reliable identification of small side peaks in the

spectrum is hampered by DDA errors [131]. Similar results have been obtained for silver nanospheres [134].

Although DDA simulations for nanoparticles mostly focus on extinction efficiency, as this is usually measured experimentally, several researchers have studied its constituents—absorption and scattering efficiencies—separately [132, 135, 136]. This should result in a better understanding of DDA errors, especially their size dependence. Moreover, absorption efficiency is relevant to practical applications involving optical heating of nanoparticles.

Recently a systematic error analysis of the DDA for gold nanoparticles was performed [67]. In the following this study is considered in details. Its important features were using a wide range of discretizations and relatively new FCD formulation, additionally to the standard LDR (see Sec. 2.4.3.2). The following particles were considered: two spheres (diameters $D = 10$ and 100 nm), two cubes (edge sizes $D = 10$ and 100 nm), and a rod (cylinder with hemispherical caps, diameter 20 nm, total length 90 nm). The incident light propagated along the z-axis and was polarized (E-field) along the x-axis. Cubes were oriented with edges along the coordinate axes, and the rod was oriented with symmetry axis along the x-axis, emphasizing the longitudinal plasmon resonance. All particles were considered in vacuum using the wavelength range [0.398,0.822] μm. The latter is informative for gold, since it contains both moderate and plasmonic $\tilde{n}$, see, e.g. Fig. 2.2. Values of $\tilde{n}$ were taken from Johnson and Christy [37] without size correction (see Sec. 2.3).

Absorption and scattering efficiencies (Q_{abs}, Q_{sca}) were calculated using ADDA 0.79 varying the discretization level, characterized by number of dipoles N_x along the x-axis. Reference results were obtained using Mie theory [46], T-matrix method [137], and extrapolation technique combined with the DDA [68] for the spheres, the rod, and the cubes respectively. Some of the results [67] for Q_{abs} and Q_{sca} are presented in Fig. 2.3 and Fig. 2.4, respectively. Since the accuracy of these two quantities weakly depends on the size [67] (see also Fig. 2.5), only results for the smaller sphere and cube are shown.

The immediate conclusion is that errors can be huge (100% and more) when using moderate N_x. On the other hand, such a

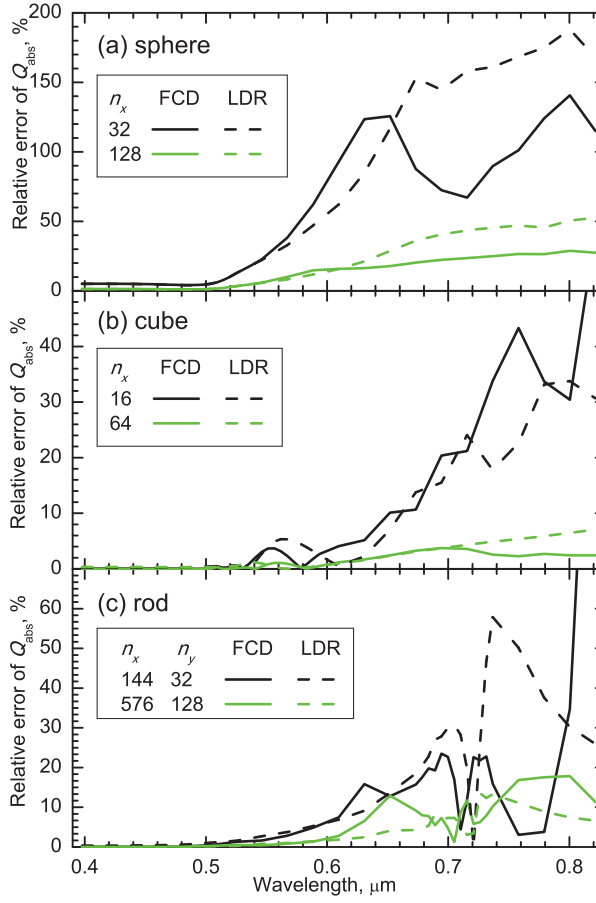

Figure 2.3 Relative errors of absorption efficiency Q_{abs} computed using the FCD and LDR formulations of the DDA, varying the number of dipoles, for gold (a) 10-nm sphere, (b) 10-nm cube, and (c) 20×90-nm rod.

reasonable task as obtaining Q_{abs} of a sphere (or a rod) in the near-IR with at least 10% accuracy requires N_x up to 256 ($N \sim 10^7$), which is still very challenging for a desktop PC, considering large N_{iter} (see Fig. 2.2) and potential need for orientational averaging. Fortunately, the errors for the cube are an order of magnitude smaller than for the sphere and the rod for the same dipole size.

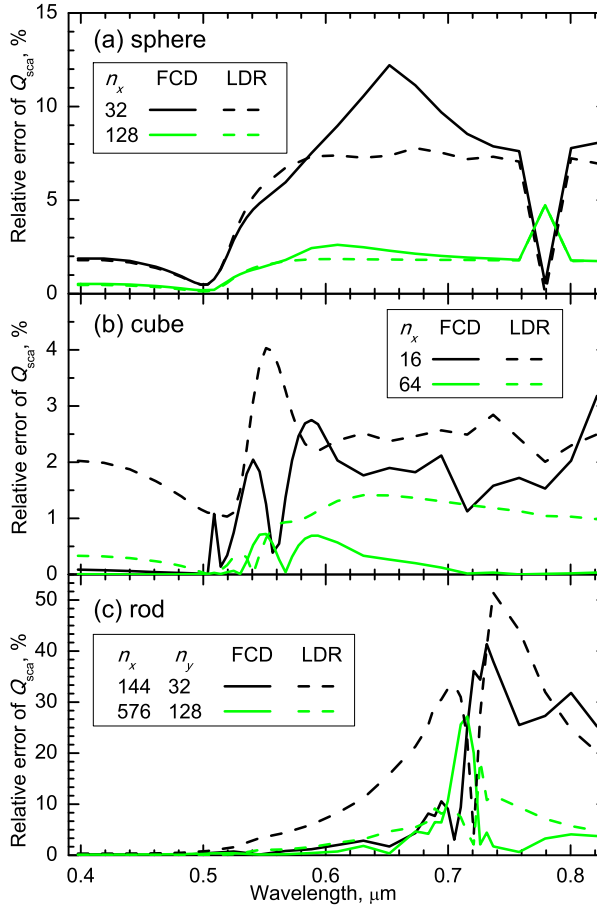

Figure 2.4 Same as Fig. 2.3 but for scattering efficiency Q_{sca}.

Supposedly, the situation is similar for other shapes that can be exactly described by a set of cubical dipoles due to absence of shape errors. Therefore, for other shapes the accuracy of DDA is expected to be significantly improved by the WD (see Sec. 2.4.3.4) or similar ideas, which calls for their implementation in the production DDA codes.

The relative errors of Q_{sca} are about 10 times less than that of Q_{abs} for the spheres and the cubes, but only 2 times for the rod. The reasons for such difference are still unclear. However, it

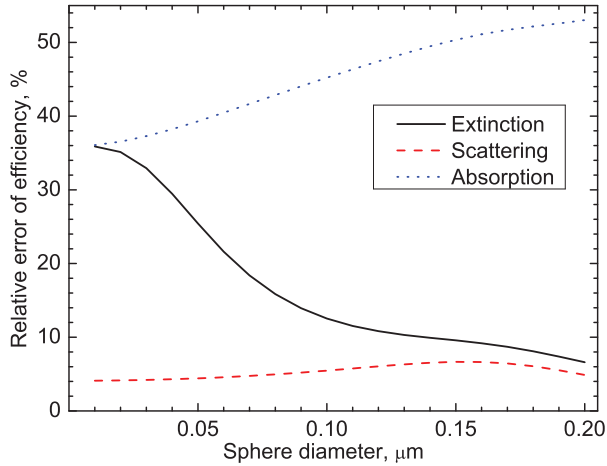

Figure 2.5 Relative errors of Q_{ext}, Q_{sca}, and Q_{abs} of a gold sphere computed using the FCD formulation of the DDA as a function of sphere diameter ($\lambda = 0.694$ μm, $N_x = 64$).

implies that accuracy of Q_{ext} has strong size dependence due to very different size dependences of Q_{abs} and Q_{sca}, which are $O(D/\lambda)$ and $O((D/\lambda)^4)$, respectively, for $D < \lambda$ [46]. In other words, accuracy of Q_{ext} is similar to that of Q_{abs} for smaller and to that of Q_{sca} for larger particles, which is illustrated in Fig. 2.5 for a specific value of λ [67]. The boundary value of D for the spheres is 50–200 nm depending on λ [67]. Therefore, accuracy of Q_{ext} can be unusually poor for sufficiently small nanoparticles, as compared to earlier studies using larger particles (e.g. 300 nm spheres, [131]).

In certain plasmonic applications the only quantity of interest is the position and the amplitude of the spectral peak. For these values the DDA accuracy is much better than that discussed above. Using moderate discretization (32 dipoles per shortest particle dimension), the position is determined with accuracy better than 10 nm and the amplitude—better than 3% (except the FCD results for the rod [67]). Comparing the two DDA formulations, neither the FCD nor the LDR can claim conclusive superiority in terms of accuracy, although the FCD is generally more accurate. However, the FCD is recommended over the LDR for general use, since this accelerates the convergence of the iterative solver up to two times (see Fig. 2.1).

To conclude, the DDA accuracy in the field of plasmonics varies in a wide range depending on particle, wavelength, measurable quantity to be simulated, and parameters of the particular DDA code. It is hard to give general recipes, because universally accurate DDA results may be too computationally expensive. Therefore, one should exercise caution when performing such simulations, as discussed in Sec. 2.5.3. Moreover, the DDA accuracy is expected to become significantly better in certain cases, if promising new DDA formulations are implemented in the production codes.

Acknowledgments

I thank Alfons Hoekstra for introducing me to a beautiful world of the DDA and for many fruitful discussions we had on this subject. I also thank David de Kanter for his invaluable contribution to the study of DDA accuracy when applied to gold nanoparticles. I acknowledge support of the program of the Russian Government "Research and educational personnel of innovative Russia" (contracts 8752 and 8804), by grant from the Russian Government 11.G34.31.0034, and of the Russian Foundation of Basic Research (grant 12-04-00737-a).

References

1. Mie, G. (1908) Beitrage zur optik truber medien, speziell kolloidaler metallosungen, *Ann. Phys. (NY)*, **330**, 377–445.
2. Mishchenko, M. I., Travis, L. D., and Lacis, A. A. (2002) *Scattering, Absorption, and Emission of Light by Small Particles*, Cambridge University Press, Cambridge.
3. Mishchenko, M. I., Hovenier, J. W., and Travis, L. D., (2000) *Light Scattering by Nonspherical Particles, Theory, Measurements, and Applications*, Academic Press, New York.
4. Mishchenko, M. I., Travis, L. D., and Mackowski, D. W. (1996) T-matrix computations of light scattering by nonspherical particles: A review, *J. Quant. Spectrosc. Radiat. Transfer*, **55**, 535–575.

5. Myroshnychenko, V., Carbó-Argibay, E., Pastoriza-Santos, I., Pérez-Juste, J., Liz-Marzán, L. M., and Garcia de Abajo, F. J. (2008) Modeling the optical response of highly faceted metal nanoparticles with a fully 3D boundary element method, *Adv. Mater.*, **20**, 4288–4293.
6. Kern, A. M., and Martin, O. J. F. (2009) Surface integral formulation for 3D simulations of plasmonic and high permittivity nanostructures, *J. Opt. Soc. Am. A*, **26**, 732–740.
7. Ungureanu, C., Rayavarapu, R. G., Manohar, S., and van Leeuwen, T. G. (2009) Discrete dipole approximation simulations of gold nanorod optical properties: Choice of input parameters and comparison with experiment, *J. Appl. Phys.*, **105**, 102032/1-7.
8. Yang, W. H., Schatz, G. C., and Vanduyne, R. P. (1995) Discrete dipole approximation for calculating extinction and Raman intensities for small particles with arbitrary shapes, *J. Chem. Phys.*, **103**, 869–875.
9. Kelly, K. L., Coronado, E., Zhao, L., and Schatz, G. C. (2003) The optical properties of metal nanoparticles: the influence of size, shape, and dielectric environment, *J. Phys. Chem. B*, **107**, 668–677.
10. Hao, F., Nehl, C. L., Hafner, J. H., and Nordlander, P. (2007) Plasmon resonances of a gold nanostar, *Nano Lett.*, **7**, 729–732.
11. Taflove, A., and Hagness, S. C. (2005) *Advances in Computational Electrodynamics: the Finite-Difference Time-Domain Method*, 3rd ed., Artech House, Boston.
12. Zhao, J., Pinchuk, A. O., McMahon, J. M., Li, S., Ausman, L. K., Atkinson, A. L., and Schatz, G. C. (2008) Methods for describing the electromagnetic properties of silver and gold nanoparticles, *Accounts Chem. Res.*, **41**, 1710–1720.
13. Monk, P. (2003) *Finite Element Methods for Maxwell's Equations*, Oxford University Press, New York.
14. Zhu, S., Zhou, W., Park, G., and Li, E. (2010) Numerical design methods of nanostructure array for nanobiosensing, *Plasmonics*, **5**, 267–271.
15. Hellmers, J., Riefler, N., Wriedt, T., and Eremin, Y. A. (2008) Light scattering simulation for the characterization of sintered silver nanoparticles, *J. Quant. Spectrosc. Radiat. Transfer*, **109**, 1363–1373.
16. Wriedt, T. (2007) Review of the null-field method with discrete sources, *J. Quant. Spectrosc. Radiat. Transfer*, **106**, 535–545.
17. Myroshnychenko, V., Rodriguez-Fernandez, J., Pastoriza-Santos, I., Funston, A. M., Novo, C., Mulvaney, P., Liz-Marzán, L. M., and Garcia de Abajo, F. J. (2008) Modelling the optical response of gold nanoparticles, *Chem. Soc. Rev.*, **37**, 1792–1805.

18. Khlebtsov, N. G., and Dykman, L. A. (2010) Optical properties and biomedical applications of plasmonic nanoparticles, *J. Quant. Spectrosc. Radiat. Transfer*, **111**, 1–35.
19. Parsons, J., Burrows, C. P., Sambles, J. R., and Barnes, W. L. (2010) A comparison of techniques used to simulate the scattering of electromagnetic radiation by metallic nanostructures, *J. Mod. Optics*, **57**, 356–365.
20. Comberg, U., and Wriedt, T. (1999) Comparison of scattering calculations for aggregated particles based on different models, *J. Quant. Spectrosc. Radiat. Transfer*, **63**, 149–162.
21. Wriedt, T., and Comberg, U. (1998) Comparison of computational scattering methods, *J. Quant. Spectrosc. Radiat. Transfer*, **60**, 411–423.
22. Gilev, K. V., Eremina, E., Yurkin, M. A., and Maltsev, V. P. (2010) Comparison of the discrete dipole approximation and the discrete source method for simulation of light scattering by red blood cells, *Opt. Express*, **18**, 5681–5690.
23. Gallinet, B., Kern, A. M., and Martin, O. J. F. (2010) Accurate and versatile modeling of electromagnetic scattering on periodic nanostructures with a surface integral approach, *J. Opt. Soc. Am. A*, **27**, 2261–2271.
24. Chaumet, P. C., Rahmani, A., and Bryant, G. W. (2003) Generalization of the coupled dipole method to periodic structures, *Phys. Rev. B*, **67**, 165404/1-5.
25. Draine, B. T., and Flatau, P. J. (2008) Discrete-dipole approximation for periodic targets: theory and tests, *J. Opt. Soc. Am. A*, **25**, 2693–2703.
26. Paulus, M., Gay-Balmaz, P., and Martin, O. J. F. (2000) Accurate and efficient computation of the Green's tensor for stratified media, *Phys. Rev. E*, **62**, 5797–5807.
27. Loke, V. L. Y., and Menguc, M. P. (2010) Surface waves and atomic force microscope probe-particle near-field coupling: discrete dipole approximation with surface interaction, *J. Opt. Soc. Am. A*, **27**, 2293–2303.
28. Schmehl, R., Nebeker, B. M., and Hirleman, E. D. (1997) Discrete-dipole approximation for scattering by features on surfaces by means of a two-dimensional fast Fourier transform technique, *J. Opt. Soc. Am. A*, **14**, 3026–3036.
29. Wijers, C. (1986) Rayleigh scattering from single-site polysylane adsorbed on silicon: Theory, *Surf. Sci.*, **168**, 816–822.
30. Taubenblatt, M. A., and Tran, T. K. (1993) Calculation of light-scattering from particles and structures on a surface by the coupled-dipole method, *J. Opt. Soc. Am. A*, **10**, 912–919.

31. Mackowski, D. W. (2010) A generalization of image theory to predict the interaction of multipole fields with plane surfaces, *J. Quant. Spectrosc. Radiat. Transfer*, **111**, 802–809.
32. D'Agostino, S., Pompa, P. P., Chiuri, R., Phaneuf, R. J., Britti, D. G., Rinaldi, R., Cingolani, R., and Della Sala, F. (2009) Enhanced fluorescence by metal nanospheres on metal substrates, *Opt. Lett.*, **34**, 2381–2383.
33. Parviainen, H., and Lumme, K. (2008) Scattering from rough thin films: discrete-dipole-approximation simulations, *J. Opt. Soc. Am. A*, **25**, 90–97.
34. Mackowski, D. W. (2007) Direct simulation of scattering and absorption by particle deposits, in *Proceedings of the 10th Conference on Electromagnetic and Light Scattering* (ed. Videen, G., Mishchenko, M. I., and Menguc, M. P.) Bodrum, Turkey, pp. 113–116.
35. Martin, O. J. F. (2004) Efficient scattering calculations in complex backgrounds, *AEU-Int. J. Electron. Commun.*, **58**, 93–99.
36. Khlebtsov, N. G. (2008) Optics and biophotonics of nanoparticles with a plasmon resonance, *Quantum Electron.*, **38**, 504–529.
37. Johnson, P. B., and Christy, R. W. (1972) Optical constants of the noble metals, *Phys. Rev. B*, **6**, 4370–4379.
38. Palik, E. D., (ed.) (1985) *Handbook of Optical Constants of Solids*, Academic Press, San Diego.
39. http://refractiveindex.info/
40. Yurkin, M. A., and Hoekstra, A. G. (2007) The discrete dipole approximation: an overview and recent developments, *J. Quant. Spectrosc. Radiat. Transfer*, **106**, 558–589.
41. Kahnert, F. M. (2003) Numerical methods in electromagnetic scattering theory, *J. Quant. Spectrosc. Radiat. Transfer*, **79**, 775–824.
42. Lakhtakia, A. (1992) Strong and weak forms of the method of moments and the coupled dipole method for scattering of time-harmonic electromagnetic fields, *Int. J. Mod. Phys. C*, **3**, 583–603.
43. Yanghjian, A. D. (1980) Electric dyadic Green's function in the source region, *IEEE Proc.*, **68**, 248–263.
44. Draine, B. T., and Flatau, P. J. (1994) Discrete-dipole approximation for scattering calculations, *J. Opt. Soc. Am. A*, **11**, 1491–1499.
45. Goedecke, G. H., and O'Brien, S. G. (1988) Scattering by irregular inhomogeneous particles via the digitized Green's function algorithm, *Appl. Optics*, **27**, 2431–2438.
46. Bohren, C. F., and Huffman, D. R. (1983) *Absorption and Scattering of Light by Small Particles*, Wiley, New York.

47. Hage, J. I., Greenberg, J. M., and Wang, R. T. (1991) Scattering from arbitrarily shaped particles: theory and experiment, *Appl. Optics*, **30**, 1141–1152.
48. Draine, B. T. (1988) The discrete dipole approximation and its application to interstellar graphite grains, *Astrophys. J.*, **333**, 848–872.
49. Hoekstra, A. G., Frijlink, M., Waters, L. B. F. M., and Sloot, P. M. A. (2001) Radiation forces in the discrete-dipole approximation, *J. Opt. Soc. Am. A*, **18**, 1944–1953.
50. Draine, B. T., and Weingartner, J. C. (1996) Radiative torques on interstellar grains .1. Superthermal spin-up, *Astrophys. J.*, **470**, 551–565.
51. Chaumet, P. C., Rahmani, A., Sentenac, A., and Bryant, G. W. (2005) Efficient computation of optical forces with the coupled dipole method, *Phys. Rev. E*, **72**, 046708/1-6.
52. Press, W. H., Flannery, B. P., Teukolsky, S. A., and Vetterling, W. T. (1990) *Numerical Recipes in C. The Art of Scientific Computing*, Cambridge University Press, New York.
53. Barrett, R., Berry, M., Chan, T. F., Demmel, J., Donato, J., Dongarra, J., Eijkhout, V., Pozo, R., Romine, C., and van der Vorst, H. A. (1994) *Templates for the Solution of Linear Systems: Building Blocks for Iterative Methods*, 2nd ed., SIAM, Philadelphia.
54. Purcell, E. M., and Pennypacker, C. R. (1973) Scattering and adsorption of light by nonspherical dielectric grains, *Astrophys. J.*, **186**, 705–714.
55. Hoekstra, A. G., Grimminck, M. D., and Sloot, P. M. A. (1998) Large scale simulations of elastic light scattering by a fast discrete dipole approximation, *Int. J. Mod. Phys. C*, **9**, 87–102.
56. Rahola, J. (1996) Solution of dense systems of linear equations in the discrete-dipole approximation, *SIAM J. Sci. Comput.*, **17**, 78–89.
57. Flatau, P. J. (1997) Improvements in the discrete-dipole approximation method of computing scattering and absorption, *Opt. Lett.*, **22**, 1205–1207.
58. Fan, Z. H., Wang, D. X., Chen, R. S., and Yung, E. K. N. (2006) The application of iterative solvers in discrete dipole approximation method for computing electromagnetic scattering, *Microw. Opt. Techn. Lett.*, **48**, 1741–1746.
59. Yurkin, M. A., Maltsev, V. P., and Hoekstra, A. G. (2007) The discrete dipole approximation for simulation of light scattering by particles much larger than the wavelength, *J. Quant. Spectrosc. Radiat. Transfer*, **106**, 546–557.

60. Lumme, K., and Rahola, J. (1994) Light-scattering by porous dust particles in the discrete-dipole approximation, *Astrophys. J.*, **425**, 653–667.
61. Freund, R. W., and Nachtigal, N. M. (1994) An implementation of the QMR method based on coupled 2-term recurrences, *SIAM J. Sci. Comput.*, **15**, 313–337.
62. Garcia, M. D., Florez, E., Suarez, A., Gonzalez, L., and Montero, G. (2005) New implementation of QMR-type algorithms, *Comp. Struct.*, **83**, 2414–2422.
63. Gutknecht, M. H., and Strakos, Z. (2000) Accuracy of two three-term and three two-term recurrences for Krylov space solvers, *SIAM J. Matrix Anal. Appl.*, **22**, 213–229.
64. Freund, R. W. (1992) Conjugate gradient-type methods for linear systems with complex symmetrical coefficient matrices, *SIAM J. Sci. Stat. Comp.*, **13**, 425–448.
65. Yurkin, M. A. and Hoekstra, A. G. (2011) The discrete-dipole-approximation code ADDA: capabilities and known limitations, *J. Quant. Spectrosc. Radiat. Transfer*, **112**, 2234–2247.
66. Rahola, J. (2000) On the eigenvalues of the volume integral operator of electromagnetic scattering, *SIAM J. Sci. Comput.*, **21**, 1740–1754.
67. Yurkin, M. A., de Kanter, D., and Hoekstra, A. G. (2010) Accuracy of the discrete dipole approximation for simulation of optical properties of gold nanoparticles, *J. Nanophotonics*, **4**, 041585/1–15.
68. Yurkin, M. A., Maltsev, V. P., and Hoekstra, A. G. (2006) Convergence of the discrete dipole approximation. II. An extrapolation technique to increase the accuracy, *J. Opt. Soc. Am. A*, **23**, 2592–2601.
69. Budko, N. V., Samokhin, A. B., and Samokhin, A. A. (2005) A generalized overrelaxation method for solving singular volume integral equations in low-frequency scattering problems, *Diff. Equat.*, **41**, 1262–1266.
70. Rakic, A. D. (1995) Algorithm for the determination of intrinsic optical constants of metal films: application to aluminum, *Appl. Optics*, **34**, 4755–4767.
71. Budko, N. V., and Samokhin, A. B. (2006) Spectrum of the volume integral operator of electromagnetic scattering, *SIAM J. Sci. Comput.*, **28**, 682–700.
72. Ayranci, I., Vaillon, R., and Selcuk, N. (2007) Performance of discrete dipole approximation for prediction of amplitude and phase of electromagnetic scattering by particles, *J. Quant. Spectrosc. Radiat. Transfer*, **103**, 83–101.

73. Flatau, P. J. (2004) Fast solvers for one dimensional light scattering in the discrete dipole approximation, *Opt. Express*, **12**, 3149–3155.
74. Flatau, P. J., Stephens, G. L., and Draine, B. T. (1990) Light-scattering by rectangular solids in the discrete-dipole approximation – a new algorithm exploiting the block-Toeplitz structure, *J. Opt. Soc. Am. A*, **7**, 593–600.
75. Goodman, J. J., Draine, B. T., and Flatau, P. J. (1991) Application of fast-Fourier-transform techniques to the discrete-dipole approximation, *Opt. Lett.*, **16**, 1198–1200.
76. Barrowes, B. E., Teixeira, F. L., and Kong, J. A. (2001) Fast algorithm for matrix-vector multiply of asymmetric multilevel block-Toeplitz matrices in 3-D scattering, *Microw. Opt. Techn. Lett.*, **31**, 28–32.
77. Greengard, L., and Rokhlin, V. (1987) A fast algorithm for particle simulations, *J. Comput. Phys.*, **73**, 325–348.
78. Rahola, J. (1996) Diagonal forms of the translation operators in the fast multipole algorithm for scattering problems, *BIT*, **36**, 333–358.
79. Hoekstra, A. G., and Sloot, P. M. A. (1994) New computational techniques to simulate light-scattering from arbitrary particles, *Part. Part. Sys. Charact.*, **11**, 189–193.
80. Taboada, J. M., Landesa, L., Obelleiro, F., Rodriguez, J. L., Bertolo, J. M., Araujo, M. G., Mourino, J. C., and Gomez, A. (2009) High scalability FMM-FFT electromagnetic solver for supercomputer systems, *IEEE Antennas Propag. Mag.*, **51**, 20–28.
81. Dembart, B., and Yip, E. (1998) The accuracy of fast multipole methods for Maxwell's equations, *IEEE Comp. Sci. Engin.*, **5**, 48–56.
82. Darve, E. (2000) The fast multipole method I: error analysis and asymptotic complexity, *SIAM J. Numer. Anal.*, **38**, 98–128.
83. Koc, S., and Chew, W. C. (2001) Multilevel fast multipole algorithm for the discrete dipole approximation, *J. Electromagnet. Wave.*, **15**, 1447–1468.
84. Singham, M. K., Singham, S. B., and Salzman, G. C. (1986) The scattering matrix for randomly oriented particles, *J. Chem. Phys.*, **85**, 3807–3815.
85. Lou, W., and Charalampopoulos, T. T. (1994) On the electromagnetic scattering and absorption of agglomerated small spherical particles, *J. Phys. D. Appl. Phys.*, **27**, 2258–2270.
86. McClain, W. M., and Ghoul, W. A. (1986) Elastic light scattering by randomly oriented macromolecules: Computation of the complete set of observables, *J. Chem. Phys.*, **84**, 6609–6622.

87. Khlebtsov, N. G. (2001) Orientational averaging of integrated cross sections in the discrete dipole method, *Opt. Spectrosc.*, **90**, 408–415.
88. Mackowski, D. W., and Mishchenko, M. I. (1996) Calculation of the T matrix and the scattering matrix for ensembles of spheres, *J. Opt. Soc. Am. A*, **13**, 2266–2278.
89. Mishchenko, M. I. (1993) Light-scattering by size shape distributions of randomly oriented axially-symmetrical particles of a size comparable to a wavelength, *Appl. Opt.*, **32**, 4652–4666.
90. Mackowski, D. W. (2002) Discrete dipole moment method for calculation of the T matrix for nonspherical particles, *J. Opt. Soc. Am. A*, **19**, 881–893.
91. Simoncini, V. (1997) A stabilized QMR version of block BICG, *SIAM J. Matrix Anal. Appl.*, **18**, 419–434.
92. Freund, R. W., and Malhotra, M. (1997) A block QMR algorithm for non-Hermitian linear systems with multiple right-hand sides, *Linear Algebra Appl.*, **254**, 119–157.
93. Boyse, W. E., and Seidl, A. A. (1996) A block QMR method for computing multiple simultaneous solutions to complex symmetric systems, *SIAM J. Sci. Comput.*, **17**, 263–274.
94. Okada, Y., Mann, I., Sano, I., and Mukai, S. (2008) Acceleration of the iterative solver in the discrete dipole approximation: Application to the orientation variation of irregularly shaped particles, *J. Quant. Spectrosc. Radiat. Transfer*, **109**, 1461–1473.
95. Draine, B. T., and Flatau, P. J. (2012) User guide for the discrete dipole approximation code DDSCAT 7.2. http://arXiv.org/abs/1202.3424.
96. Okada, Y. (2008) Efficient numerical orientation averaging of light scattering properties with a quasi-Monte-Carlo method, *J. Quant. Spectrosc. Radiat. Transfer*, **109**, 1719–1742.
97. Muinonen, K., and Zubko, E. (2006) Optimizing the discrete-dipole approximation for sequences of scatterers with identical shapes but differing sizes or refractive indices, *J. Quant. Spectrosc. Radiat. Transfer*, **100**, 288–294.
98. Yurkin, M. A., Min, M., and Hoekstra, A. G. (2010) Application of the discrete dipole approximation to very large refractive indices: Filtered coupled dipoles revived, *Phys. Rev. E*, **82**, 036703/1–12.
99. Budko, N. V., and Remis, R. F. (2004) Electromagnetic inversion using a reduced-order three-dimensional homogeneous model, *Inverse Probl.*, **20**, S17–S26.

100. Draine, B. T., and Goodman, J. J. (1993) Beyond Clausius–Mossotti – wave-propagation on a polarizable point lattice and the discrete dipole approximation, *Astrophys. J.*, **405**, 685–697.
101. Chaumet, P. C., Sentenac, A., and Rahmani, A. (2004) Coupled dipole method for scatterers with large permittivity, *Phys. Rev. E*, **70**, 036606/1–6.
102. Piller, N. B., and Martin, O. J. F. (1998) Increasing the performance of the coupled-dipole approximation: A spectral approach, *IEEE Trans. Antennas Propag.*, **46**, 1126–1137.
103. Piller, N. B. (1999) Coupled-dipole approximation for high permittivity materials, *Opt. Commun.*, **160**, 10–14.
104. Yurkin, M. A., Maltsev, V. P., and Hoekstra, A. G. (2006) Convergence of the discrete dipole approximation. I. Theoretical analysis, *J. Opt. Soc. Am. A*, **23**, 2578–2591.
105. Jackson, J. D. (1975) *Classical Electrodynamics*, 2nd edn, Wiley, New York.
106. Hage, J. I., and Greenberg, J. M. (1990) A model for the optical properties of porous grains, *Astrophys. J.*, **361**, 251–259.
107. Lakhtakia, A., and Mulholland, G. W. (1993) On 2 numerical techniques for light-scattering by dielectric agglomerated structures, *J. Res. Nat. Inst. Stand. Technol.*, **98**, 699–716.
108. Peltoniemi, J. I. (1996) Variational volume integral equation method for electromagnetic scattering by irregular grains, *J. Quant. Spectrosc. Radiat. Transfer*, **55**, 637–647.
109. Gutkowicz-Krusin, D., and Draine, B. T. (2004) Propagation of electromagnetic waves on a rectangular lattice of polarizable points. http://arxiv.org/abs/astro-ph/0403082.
110. Rahmani, A., Chaumet, P. C., and Bryant, G. W. (2002) Coupled dipole method with an exact long-wavelength limit and improved accuracy at finite frequencies, *Opt. Lett.*, **27**, 2118–2120.
111. Collinge, M. J., and Draine, B. T. (2004) Discrete-dipole approximation with polarizabilities that account for both finite wavelength and target geometry, *J. Opt. Soc. Am. A*, **21**, 2023–2028.
112. Rahmani, A., Chaumet, P. C., and Bryant, G. W. (2004) On the importance of local-field corrections for polarizable particles on a finite lattice: Application to the discrete dipole approximation, *Astrophys. J.*, **607**, 873–878.
113. Dungey, C. E., and Bohren, C. F. (1991) Light-scattering by nonspherical particles: a refinement to the coupled-dipole method, *J. Opt. Soc. Am. A*, **8**, 81–87.

114. Doyle, W. T. (1989) Optical properties of a suspension of metal spheres, *Phys. Rev. B*, **39**, 9852–9858.
115. Okamoto, H. (1995) Light scattering by clusters: the a1-term method, *Opt. Rev.*, **2**, 407–412.
116. Piller, N. B. (1997) Influence of the edge meshes on the accuracy of the coupled-dipole approximation, *Opt. Lett.*, **22**, 1674–1676.
117. McDonald, J., Golden, A., and Jennings, S. G. (2009) OpenDDA: a novel high-performance computational framework for the discrete dipole approximation, *Int. J. High Perf. Comp. Appl.*, **23**, 42–61.
118. Yurkin, M. A., Hoekstra, A. G., Brock, R. S., and Lu, J. Q. (2007) Systematic comparison of the discrete dipole approximation and the finite difference time domain method for large dielectric scatterers, *Opt. Express*, **15**, 17902–17911.
119. Penttila, A., Zubko, E., Lumme, K., Muinonen, K., Yurkin, M. A., Draine, B. T., Rahola, J., Hoekstra, A. G., and Shkuratov, Y. (2007) Comparison between discrete dipole implementations and exact techniques, *J. Quant. Spectrosc. Radiat. Transfer*, **106**, 417–436.
120. http://groups.google.com/group/adda-discuss.
121. http://openmp.org/.
122. http://www.mpi-forum.org/.
123. http://www.astro.princeton.edu/~draine/DDSCAT.html.
124. http://code.google.com/p/a-dda/.
125. Yurkin, M. A., and Hoekstra, A. G. (2012) User manual for the discrete dipole approximation code ADDA v.1.1. http://a-dda.googlecode.com/svn/tags/rel_1.1/doc/manual.pdf.
126. Flatau, P. J. and Draine, B. T. (2012) Fast near field calculations in the discrete dipole approximation for regular rectilinear grids, *Opt. Express*, **20**, 1247–1252.
127. Yurkin, M. A. and Kahnert, M. (2013) Light scattering by a cube: accuracy limits of the discrete dipole approximation and the T-matrix method, *J. Quant. Spectrosc. Radiat. Transfer*, http://dx.doi.org/10.1016/j.jqsrt.2012.10.001.
128. Pecharroman, C., Perez-Juste, J., Mata-Osoro, G., Liz-Marzán, L. M., and Mulvaney, P. (2008) Redshift of surface plasmon modes of small gold rods due to their atomic roughness and end-cap geometry, *Phys. Rev. B*, **77**, 035418/1–7.
129. Hao, E., Schatz, G., and Hupp, J. (2004) Synthesis and optical properties of anisotropic metal nanoparticles, *J. Fluoresc.*, **14**, 331–341.

130. Kooij, E. S., and Poelsema, B. (2006) Shape and size effects in the optical properties of metallic nanorods, *Phys. Chem. Chem. Phys.*, **8**, 3349–3357.
131. Shuford, K. L., Ratner, M. A., and Schatz, G. C. (2005) Multipolar excitation in triangular nanoprisms, *J. Chem. Phys.*, **123**, 114713/ 1–9.
132. Lee, K., and El-Sayed, M. A. (2005) Dependence of the enhanced optical scattering efficiency relative to that of absorption for gold metal nanorods on aspect ratio, size, end-cap shape, and medium refractive index, *J. Phys. Chem. B*, **109**, 20331–20338.
133. Yang, P., Portals, H., and Pileni, M. (2009) Identification of multipolar surface plasmon resonances in triangular silver nanoprisms with very high aspect ratios using the DDA method, *J. Phys. Chem. C*, **113**, 11597–11604.
134. Jensen, T., Kelly, L., Lazarides, A., and Schatz, G. C. (1999) Electrodynamics of noble metal nanoparticles and nanoparticle clusters, *J. Clust. Sci.*, **10**, 295–317.
135. Sosa, I. O., Noguez, C., and Barrera, R. G. (2003) Optical properties of metal nanoparticles with arbitrary shapes, *J. Phys. Chem. B*, **107**, 6269–6275.
136. Jain, P. K., Lee, K. S., El-Sayed, I. H., and El-Sayed, M. A. (2006) Calculated absorption and scattering properties of gold nanoparticles of different size, shape, and composition: applications in biological imaging and biomedicine, *J. Phys. Chem. B*, **110**, 7238–7248.
137. Mishchenko, M. I., and Travis, L. D. (1998) Capabilities and limitations of a current FORTRAN implementation of the T-matrix method for randomly oriented, rotationally symmetric scatterers, *J. Quant. Spectrosc. Radiat. Transfer*, **60**, 309–324.